Pressure, temperature and timing of mineralization of the sedimentary rock-hosted orogenic gold deposit at Klipwal, southeastern Kaapvaal Craton, South Africa

Sakthi Saravanan Chinnasamy[1*$], Ron Uken[1#] Jürgen Reinhardt[1], David Selby [2], Spencer Johnson[3]

[1]School of Agricultural, Earth and Environmental Sciences, Discipline of Geological Sciences, University of KwaZulu-Natal, Westville Campus, Durban 4000, South Africa

[2]Department of Earth Sciences, University of Durham, Durham DH1 3LE, UK

[3]No 326, Canterbury Ct., Alamo, CA, 94507, USA

*Corresponding author e-mail:geosaks@gmail.com

[$]Present address:
Department of Earth Sciences, CEMPEG, Uppsala University, Villavagen 16, SE-75236 Uppsala, Sweden

[#] Present address:
17 N. Grosvenor Ave, Burnaby, V5B1J1, BC, Canada

Abstract

Gold mineralization in the Klipwal Shear Zone (KSZ) at the Klipwal Gold Mine is confined to laminated quartz-carbonate lodes, stringers and associated alteration in sandstone and siltstone of the Delfkom Formation in the upper Mozaan Group of the Mesoarchaean Pongola Supergroup. The moderately dipping brittle-ductile KSZ strikes N-S with an oblique-reverse, sinistral sense of shear. The deformational events that are recognized include an early compressional phase that produced anastomosing shears defined by shear fabrics with numerous shear-parallel laminated quartz-carbonate fault-fill veins and, in places, extensional quartz vein stockworks, and a late brittle reactivation phase that produced fault breccias, displacing earlier extensional veins. Three closely spaced economic reefs (lodes) are developed: the main R-reef constitutes the KSZ, while the J- and H- reefs represent footwall splays. Alteration comprises chlorite, muscovite, epidote, feldspar and carbonates along with pyrite, arsenopyrite and chalcopyrite ± pyrrhotite. An inner

alteration zone is dominated by laminated quartz-carbonate veins with alternating quartz-carbonate-rich and muscovite-chlorite-rich laminae whereas the proximal zone is characterized by alteration halos of K-feldspar, albite, epidote, chlorite and muscovite along with carbonates and associated quartz veins. Chlorite thermometry from the inner and proximal zone yielded temperatures of 267 to 312 °C. Arsenopyrite compositions provide temperatures in the same range, 255 to 318 °C. Fluid inclusion microthermometry and Raman spectrometry of quartz veins in the mineralized reefs reveal the presence of metamorphogenic aqueous-gaseous fluid with an average salinity of 6.5 wt. % NaCl equiv. Fluid compositions and estimated P–T range (1.1 to 2.5 kbar at 255 to 318 °C) are typical of orogenic gold deposits. Devolatilization during the regional facies metamorphism of the Pongola Supergroup is considered the likely fluid forming event with fluid flow focused into a 'compressional-jog' of the KSZ. Shear-induced pressure fluctuations generated phase separation of the initial aqueous gaseous fluid producing a gaseous and low saline aqueous fluid. This, together with fluid–rock interaction, and a decrease in fO_2 lead to sulphide and gold precipitation at Klipwal. Re-Os data from six sulfide samples constrain the age of sulfide precipitation and, by inference, gold mineralization, to 2563 ± 84 Ma, with an initial $^{187}Os/^{188}Os$ = 0.29 ± 0.08 (MSWD = 0.38). This age is distinctly younger than the post-Pongola granites (2863–2721 Ma) ruling out the association of granite emplacement with mineralization. This would suggest that mineralization is linked to the regional D_3 folding event which reactivated the KSZ after emplacement of the post-Pongola granites and that final brittle, post-mineralization reactivation is related to Karoo-age faulting. Low initial Os values suggest that ore fluid interacted with mafic rocks, leaching non-radiogenic Os, the likely source being the deeper-seated Nsuze Group volcanics and/or the greenstone belts that underlie the Pongola Supergroup.

Keywords: Orogenic gold deposits, Fluid inclusions, Klipwal, Kaapvaal craton, South Africa

Introduction

Orogenic gold mineralization constitutes an important class of deposits, collectively representing a significant world gold resource (about 25000 t gold; Goldfarb et al.

2005). Although these ores are associated with deformed metamorphic terrains of almost all ages (Kerrich and Cassidy 1994) they mostly occur in the Archaean greenstone belts of Australia, Canada, Africa, India and Brazil, the Proterozoic belts of West Africa, and to a lesser extent, in Mesozoic and Cenozoic provinces (Kerrich and Cassidy 1994; Goldfarb et al. 2001; Groves et al 2003; Hagemann and Brown 2000). They are characterized by a strong structural control, distinct alteration assemblages, ore mineralogy, ore fluid composition, and occur in a range of host lithologies (Groves et al. 1998; McCuaig and Kerrich 1998; Goldfarb et al. 2001; Groves et al. 2003). These include greenstones (metamorphosed from low greenschist facies to granulite facies), banded iron-formations, ultramafic rocks, sedimentary rocks and granitoids (McCuaig and Kerrich 1998, and references therein). Among all these, sedimentary rock-hosted orogenic lode gold deposits form an important and distinctive class (Bierlein and Crowe 2000).

Although the sedimentary rock-hosted deposits are well known from the Phanerozoic there are only a handful from the Archaean, which in many ways are similar in mineralization and structural style, alteration and ore mineralogy to the Phanerozoic counterparts. These deposits, also called slate belt-hosted gold deposits, are developed in mineralized shear zones in thick marine sedimentary sequences commonly underlain by bimodal volcanics generated during spreading, arc formation, plate collision and subduction (Goldfarb et al. 1998). They are associated with major translithospheric structures or compressional to transpressional-transtensional shear zones, similar to the Archaean orogenic gold deposits (Bierlein and Crowe 2000; Lawley et al. 2013).

Sedimentary rock-hosted orogenic gold deposits are reported from a number of Phanerozoic accretionary terrains, notably the Pacific rim: the North American Cordillera, far east Russia, northeastern China, eastern Australia and New Zealand (Fig. 1 in Goldfarb et al. 1998; Bierlein and Crowe 2000). Some of the major gold-bearing districts in the eastern and western part of the Pacific rim include the Hodgkinson gold field in the Hodgkinson–Broken River Fold Belt and Ballarat in the Lachlan Fold Belt from eastern Australia (Phillips and Hughes 1996; Peters et al 1990); the Alaska–Juneau, Treadwell, Kensington mines in the Juneau gold belt in the North American Cordillera (Goldfarb et al. 1991; Miller et al. 1995), the Omchak goldfield in the Yana-Kolyma belt in northeastern Russia (Nokleberg et al. 1994;

Nokleberg et al. 1996), and the Reefton goldfield in eastern New Zealand (Cooper and Tulloch 1992; Goldfarb et al. 1995).

The sedimentary rock-hosted lode gold deposits in eastern Australia are similar in some aspects to the Klipwal gold deposit described here. Gold-bearing quartz veins in the Hodgkinson gold field, Queensland Australia, are found in low-grade metasediments with restricted hydrothermal alteration halos. Mineralization is concentrated in brittle to brittle-ductile shear zones that occur within reactivated second-generation fold axial planes (Peters et al. 1990). Geological characteristics, isotopic data, alteration mineralogy, and fluid inclusion studies show that upward migrating homogeneous metamorphic or distal magmatic fluids were responsible for the gold mineralization (Peters et al. 1990). The Ballarat East gold field is located in close proximity to the Avoca fault (Fairmaid et al. 2011) with gold hosted in large fault-related quartz veins that are stacked in arrays associated with west-dipping reverse faults. Evidence of mixing metamorphogenic fluid with sedimentary formation waters is documented by Fairmaid et al. (2011). The sources of gold are considered to include the underlying Cambrian volcanic rocks, surrounding Paleozoic sediments and Proterozoic continental crust.

In South Africa, the Mesoarchaean volcano-sedimentary sequence of the Pongola Supergroup, exposed in the southeastern part of the Kaapvaal craton (Fig. 1a), is considered contemporaneous with the Witwatersrand Supergroup and similarly contains paleo-placer Au-U conglomerate occurrences (Bullen et al. 1994). In addition to Witwatersrand type paleo-placer deposits, the Pongola Supergroup hosts a number of epigenetic, structurally controlled orogenic-style lode gold deposits (Fig. 1b). These include the Wonder Mine situated in the Bumbeni Shear Zone, the Klipwal Gold Mine (KGM) on the Klipwal Shear Zone (KSZ) and Ngotshe Mine located a few hundred meters east of the KSZ (Bullen et al. 1994). As opposed to the Pongola paleo-placer deposits the lode gold deposits have until recently continuously produced gold, especially from the Klipwal Gold Mine (Bullen et al. 1994; Gold 1993; Gold 2006). Presently the mine is not in operation.

Here we present a detailed description of the geology of the Klipwal gold deposit, its alteration mineralogy, P-T conditions of mineralization deduced from chlorite and arsenopyrite geothermometry and fluid inclusion studies on mineralized zones (reefs). In addition, we present Re-Os compositions of pyrite and arsenopyrite from the ore and report on the timing of gold mineralization. The Klipwal Gold Mine

(KGM) is located in KwaZulu-Natal Province of South Africa, about 15 km south of the Swaziland border, between the towns of Piet Retief and Pongola (Figs. 1a, b). Mining operations commenced during the late nineteenth century with a total gold production of 5.7 tons by 2003. A total of 1.18 million tons of ore were mined between 1981 and 2003, and from these, at least 5.3 tons of gold were recovered at a grade of 4.5 g/t. Mining operations extended fifteen levels to a depth of 454 m. This study is based mainly on samples collected from levels six through to ten.

Regional geological setting

The Pongola Supergroup is preserved as two structural basins, the extensive Pongola basin in the north and the smaller Nkandla basin in the south, separated by the Babanango structural high within a stabilized segment of the southeastern Kaapvaal craton (Matthews 1990; Gold 1993; Gold and Von Veh 1995; Gold 2006). The basins comprise a lower volcano-sedimentary sequence, the Nsuze Group and an upper dominantly sedimentary sequence, the Mozaan Group. The Nsuze Group is characterized by 4.6 km of mafic and subordinate felsic volcanic rocks with minor calcareous and siliciclastic sedimentary units. The overlying Mozaan Group, with a maximum thickness of 5 km, comprises arenaceous and iron-rich argillaceous sediments with minor banded ironstones. The Mozaan Group hosts both the placer and lode gold deposits, with the KSZ the most important, displacing interbedded sandstone, mudstone, ferruginous siltstone and two diamictite units of the Delfkom Formation of the Odwaleni Subgroup (Fig. 1c).

Structure

The Pongola Supergroup in the central and main Pongola basin is gently deformed and typically metamorphosed under sub-greenschist to greenschist facies conditions, with the exception of high-grade occurrences in Swaziland where granulite facies conditions had been reached locally (Wilson and Jackson 1988; Gold and Von Veh 1995; Saggerson and Turner 1995, Mukasa et al. 2013; Horvath et al. 2014). Gold and Von Veh (1995) in accordance with Matthews (1990) proposed three regional deformational events (D_1, D_2 and D_3) affecting the main Pongola basin (Fig. 1). D_1 is represented by early NNW-directed thrusts, reverse faults and shear zones, including

the KSZ (Fig. 1). During D_1, ENE-trending F_1 folds developed contemporaneously with NNW-directed thrusting. Following D_1 compressional tectonics, the area was affected by NW-SE extension (D_2) associated with the emplacement of mafic dykes and sills. This was followed by D_3 NE-SW-directed compression which produced major northwesterly trending, open upright F_3 folds that deformed the early D_1 shears and refolded the ENE-trending F_1 folds forming a dome-and-basin interference pattern (Gold and Von Veh 1995). Between D_2 and D_3 a number of granitoid plutons intruded into the Pongola Supergroup, collectively known as the post-Pongola granites (Gold 2006).

The KSZ is interpreted by Gold (2006) as a D_1 structure. It forms a major shear zone extending approximately N-S for about 20 km, characterized by a moderately dipping brittle-ductile shear plane that displays oblique-reverse sinistral sense of shear. The shear zone shows anastomosing shear fabrics with numerous shear-parallel laminated quartz-carbonate veins and, in places, a quartz-vein stockwork. There is also evidence of late brittle reactivation of the shear plane (Gold 2006).

Geochronology of granitoids

The ages of deformation and low-grade regional metamorphism remain poorly constrained due to the lack of reliable age data, whereas the geochronology of basement rocks to the Pongola Supergroup and the post-Pongola granites is well established. The basement granitoid rocks of the Anhalt granitoid suite intruded into 3300 Ma old greenstone remnants (such as the Nondweni greenstone fragment) in the southeastern Kaapvaal craton (Farrow et al. 1990; Hunter et al. 1992; Robb et al. 2006). These granitoids range in age from 3290 to 3028 Ma (Rb-Sr: Barton et al. 1983; Farrow et al. 1990; Matthews et al. 1989; U-Pb: Kamo and Davis 1994). The pre-Pongola Tsawela gneiss on the northern side of the Pongola basin formed at 3428±22 Ma (U-Pb single zircon: Mukasa et al. 2013). The Nsuze Group volcanic rocks, which non-conformably overlie the basement, were erupted between 2984±3 Ma (U-Pb single zircon: Hegner et al. 1993) and 2940±22 Ma (U-Pb: Hegner et al. 1984). On the basis of new U-Pb zircon age data, Mukasa et al. (2013) established the period of deposition for the Pongola sequence rocks. Accordingly, the oldest Nsuze group volcanic layers date at 2980± 10 Ma, which is similar to the previously

published ages, and the uppermost sedimentary layers of the Mozaan group have an age of 2954±9 Ma. The post-Pongola granitoids (cf. Fig. 1b) were emplaced over a period of about 150 Ma, between 2863 and 2721 Ma. The Godlwayo granite has been dated at 2863±8 Ma (Reimold et al. 1993), the Nzimane granite in the Hlabisa area at 2739±3 Ma (Thomas et al. 1995) and the Spekboom granite at 2700–2730 Ma (Reimold et al. 1993). Maphalala and Kröner (1993) obtained an age of 2722 ± 6 Ma for the Kwetta Granite. All these ages were obtained from single zircon Pb-evaporation method. Mukasa et al. (2013) constrained the emplacement ages for Kwetta and Mswati granites, using U-Pb zircon studies, at 2721± 10 Ma and 2723±7 Ma respectively.

Geology of the Klipwal Gold Mine

Wall rocks, structures and distribution of the reefs

The Klipwal Shear Zone cuts the Delfkom Formation of the upper Mozaan Group which comprises interbedded sandstone, siltstone, mudstone, diamictite and associated mafic and ultramafic intrusives, possibly related to the ca. 2.8 Ga Usushwana intrusive event. Gold mineralization at the KGM is centered on a convex-westward flexure in the KSZ (Fig. 1c). At least three closely spaced economic reefs are developed (Fig. 2a). The main R-reef constitutes the master shear zone while the J- and H- reefs are lodes that occupy footwall splays of varying dip. The fourth Quartz (Q)- reef is less extensive and developed as a footwall splay of the R-reef in the upper levels (Fig. 2a). The Q-reef and a major portion of the R-reef are mostly mined out. The R-reef is a curvy-planar structure dipping steeply (about 70°) in the upper levels, while gradually changing to a gentle dip at deeper levels, to as little as 35°. The most pervasive fabric observed within the KSZ is an N-S trending shear foliation which is best observed underground as it is poorly exposed on the surface. The observed structures constitute an early-formed set indicating compression, which includes the main shear zone, its mylonitic wall rocks, fault-fill veins and sub-horizontal extensional veins. A late phase of brittle faulting of the extensional veins produced a fault breccia. Poles to the major shear foliation show a point maximum corresponding to a mean strike of 014° and a dip angle of 50°E. The bulk of the variation in shear foliation orientation is within a dip direction interval from about E to ESE, and a dip

angle range between shallow and moderately steep angles. Some deviation of the shallow-dipping sections to more southerly dips and a corresponding clockwise rotation of the strike are evident in the plot of Figure 2b. The relatively well-defined pole maximum in Figure 2b, however, partly reflects a bias in the readings being taken at underground levels accessible for this study. This effectively reduces the spread of the dip and strike data expected over the entire fault structure.

Old mine excavations of the Q-reef at the surface show that the footwall comprises altered siltstone (quartz–chlorite–carbonate±muscovite–schist) and sandstone (metapsammite) in the hanging wall (Fig. 3a). Henceforth, these two rocks are named chlorite-carbonate schist and metapsammite, respectively. Although the shear fabric is not often observed on surface, reactivation of the shear plane is evident from slickensides (Fig. 3b). Shear-related folds, with a NW trending axial planar fabric, are observed in the siltstone (Fig. 3c). Strongly foliated sandstone occurs in close proximity to the shear zone (Fig. 3d).

The R-reef comprises a 0.5–5.5 m wide, strongly foliated zone, containing numerous shear-parallel fault-fill laminated quartz veins that range in thickness from less than 1 cm to a few meters (Fig. 4a). The N-S trending foliation in the R-reef forms mylonitic fabrics and locally preserves S-C fabrics indicating a horizontal offset with a sinistral sense of shear (Figs. 4a, b). Shear lenses comprising smoky quartz grains are observed in the mylonites (Fig. 4b). In places, an array of thin subhorizontal extensional veins are observed in the R-reef (Fig. 4c). The contact between the R-reef and its hanging-wall shows evidence of late brittle reactivation indicated by clay-rich fault gouge and/or breccia (Fig. 4d). The fault breccia consists of fragments of fault-fill quartz veins as well as country rocks. Sub-horizontal extensional veins are displaced by the later brittle faults (Fig. 4e).

The H-reefs form a number of footwall splays that developed from the R-reef, linking across to a sequence of reefs known as the J-reefs (Fig. 2a). The H-reefs are similar to the R-reef in that they are also characterized by brittle-ductile shears, but were not reactivated to the same extent during later brittle faulting. The fabric in the quartz veins is less pervasive, and fault breccia is absent (Fig. 4f). A crosscut at level 10 (~350m from shaft surface) from the main R-reef, provided an opportunity to access the H- and J-reef shear zones and quartz veins underground (Fig. 5). These reefs cut across a range of footwall lithologies such as metapsammite, least-altered

sandstone and chlorite-carbonate schist that strike sub-parallel to, and dip at shallower angles than, the R-reef (Fig. 5).

J-reefs represent footwall mineralization of the H-reef shears (Hilliard 2007) where the H-reef shears cut and displace the contact between least-altered sandstone and chlorite–carbonate schist (Figs. 2a and 5). J-reef ores typically extend for a distance of between 10 and 50 m representing the amount of displacement along the H-reef. Juxtaposition of the sandstone against siltstone along the H-reef shears is considered a critical controlling factor in J-reef development.

Alteration mineralogy

Petrographic studies reveal an inner and a proximal alteration zones centered on the KSZ. The inner zone is dominated by laminated quartz-carbonate veins with alternating quartz-carbonate and muscovite-chlorite-rich layers. The proximal zone is characterized by an alteration halo of K-feldspar, albite and chlorite, along with carbonate and associated quartz veins surrounding the inner zone.

About 30 m away from the KSZ, in the upper level, sandstone in the least altered zone comprises quartz grains with less K-feldspar, plagioclase, muscovite (Fig. 6a) and minor heavy minerals such as zircon, ilmenite and titanite. The clastic components are cemented by quartz. K-feldspar and plagioclase are unaltered (Fig. 6a). A weak S_1 foliation is defined by muscovite (Fig. 6a) that is considered to have formed during the development of the KSZ. Siltstone in the least altered zone is characteristically weakly foliated with the schistosity being defined by chlorite and muscovite (Fig. 6b).

In the proximal zone the altered metapsammite consists of microcline, dolomite and magnesite, indicating potassic and carbonate alteration (Figs. 6c, d). Minor chlorite and quartz are also observed in the rock as alteration products, and albitic plagioclase is intensely altered to muscovite (Fig. 6d). Chlorite–carbonate schist in the proximal zone is derived from hydrothermal alteration and deformation of siltstone along the shear zone, producing a strong fabric defined by chlorite and muscovite (Figs. 6e, f). Other minerals in this rock include epidote and quartz.

The inner alteration zone comprises auriferous laminated quartz-carbonate veins. Alternating laminae in these veins consist predominantly of quartz-carbonate and muscovite-chlorite (Fig. 7a). Carbonates in the veins include dolomite, magnesite and

siderite. A sinistral sense of shear is observed at thin-section scale with the development of an S–C fabric in the muscovite-chlorite lamina (Fig. 7b). The fine-grained texture and strong foliation indicate that the rocks experienced mylonitization and dynamic recrystallization in the shear zone. Matrix quartz grains display bulging and recrystallized grain boundaries, with some grains displaying subgrain rotation and formation of core-and-mantle structures (Figs. 7a, b, c). These textures indicate plastic deformation at low temperatures (about 300°C; Stipp et al. 2002) and correspond to sub-greenschist facies conditions. Shear lenses consisting of quartz grains are observed in the mylonitic matrix (Fig. 7d). Broken fragments of quartz vein clasts and mylonitic clasts are very well preserved in the fault breccia (Fig. 7e). Antitaxial quartz "strain fringes" within the mylonites (Fig. 7f, g) grew on rigid pyrite and arsenopyrite grains. In addition to quartz, these strain fringes sometimes contain chlorite. The 'jigsaw-puzzle' type brittle fractures in the sulfide grains are evident of hydraulic breccia and these fractures are filled with quartz and chlorite (Fig. 7f). Silicate inclusion trails within sulfides occur parallel to the matrix shear foliation (Fig. 7g, h) which suggest that either sulfides overgrowing an existing, unmodified early S_1 foliation in the D_3 event, or on a reactivated S_1-S_3 foliation, potentially during D_3. In both cases, the sulfide growth is associated with syn-D_3. As D_3 is a reactivation, presumably makes small angle between S_1 and S_3, it is difficult to distinguish these two fabrics.

Analytical techniques

Selected thin sections were analyzed for chlorite compositions using the CAMECA SX-100 electron probe micro-analyzer (EPMA) at the DST-EPMA National facility, Department of Geology and Geophysics, IIT Kharagpur. Operating conditions for chlorite analysis were 15 kV acceleration voltages with 20 nA beam currents. The counting time was 20 to 30 s. The beam diameter was set at 1 μm. For analysis of pyrite and arsenopyrite an acceleration potential of 20 kV was used. Beam currents of 200 nA and 20 nA for was used for pyrite and arsenopyrite respectively. The counting time for Fe and S was 20s and for As 40s.-Appropriate natural and synthetic minerals were used for standardization. Raw data were corrected with the help of PAP correction program by Pouchou and Pichoir (1984). Back scattered electron (BSE)

imaging was acquired using JEOL JSM 6490 SEM at the Department of Geology and Geophysics, IIT Kharagpur.

Nine doubly polished wafers of ~200 μm thickness were prepared for fluid inclusion petrographic study. Microthermometric runs were conducted on five samples with the help of a Fluid Inc. adapted USGS gas flow microscopic heating-freezing stage, fitted on a Leica Laborlux D petrological microscope housed at Geological Sciences, University of Kwazulu-Natal, Durban. The unit operates in the temperature range of –195 °C to 700 °C, and is periodically calibrated using distilled water-ice bath (0 °C) and pure CO_2 inclusions (–56.6 °C). Phase changes were observed during heating. Fluid salinity and density values were calculated and isochores were constructed using the FLUIDS software package (Bakker 2003). For type-I inclusions the DENSITY program in package CLATHRATES (Bakker 1997) was used. Equation of state (EOS) of Duan et al. (1992a, b) and Bakker (1999) was used for salinity and density calculation and isochore construction respectively. For type-II inclusions, EOS of Jacobs and Kerrich (1980) was used for calculating density, and for isochore construction Belonoshko and Saxena (1991) was used. For type-III inclusions Thiéry et al. (1994) and Duan et al (1992a) were used for calculation of density and isochore respectively. For type-IV inclusions Bodnar (1993) was used to calculate salinity and Zhang and Frants (1987) for density. A Renishaw RM1000B laser Raman probe, attached to a Leica microscope, at the Department of Geology and Geophysics, IIT Kharagpur was used to analyze fluid inclusions. The system is equipped with edge filters to block the Rayleigh lines, confocal configuration, thermoelectrically cooled CCD detector, air-cooled laser, and associated software to acquire and evaluate the spectral data. Irradiation was by the 514.5 nm line of a continuous wave Ar-ion laser, which delivered ~ 8 mW laser power at the sample surface. The acquisition time was 60 seconds. The first order Raman band of silicon at 520 cm^{-1} was used for routine calibration. The reproducibility of the Raman wave number was set up to be ± 1 cm^{-1}. Equation (2) of Burke (2001) is used for quantitative analysis of gas species (X_{CO2} and X_{CH4}) from the respective peak areas. Raman results were also compared to the graphical methods of Thiéry et al. (1994). The observed maximum uncertainty in species composition is below 5% between these two methods.

For Re-Os analysis, sulfide minerals (pyrite and arsenopyrite) were prepared using traditional methods, crushing without metal contact, heavy liquids, FRANTZ

magnetic separation and hand picking. Re and Os abundance and isotope compositions were determined using isotope dilution negative ion thermal mass spectrometry (Selby et al. 2009). In brief, approximately ~400 mg of pyrite/arsenopyrite were dissolved with a known amount of mixed tracer solution (^{185}Re, ^{190}Os) in 8 ml of inverse *aqua regia* (1:3 mix of HCl and HNO_3) in a carius tube at 220˚C for 48 hrs. Osmium was isolated and purified from the acid solution using chloroform solvent extraction ($CHCl_3$) and micro-distillation methods. Rhenium was isolated using solvent extraction (NaOH-acetone; Cumming et al. 2013) and anion chromatography. Full procedural blanks were 0.1 ± 0.1 and 6.2 ± 5.4 ppt (1 SD; n = 2) for Os and Re, respectively, with an ^{187}Os/^{188}Os of 0.25 ± 0.02. The in-house solution standards (Re std; DROsS) analyzed during the period of these are 0.59773 ± 0.002 and 0.16093 ± 0.0002 (n = 2), respectively, which are identical to those previously reported (Cumming et al. 2012 and references therein).

Chlorite geothermometry

Chlorite compositions have been used for temperature estimation and this was done by: (1) empirical calibrations based on tetrahedral Al content and amount of octahedral vacancy (Cathelineau and Nieva 1985; Zang and Fyfe 1995), and (2) thermodynamic formulation, using intra-crystalline exchange reactions between the chlorite phase components and their temperature-pressure dependence (Vidal et al. 2001; 2005). In the latter thermodynamic model four end members are considered: clinochlore [$Si_3Al_2Mg_5O_{10}(OH)_8$], daphnite [$Si_3Al_2Fe_5O_{10}(OH)_8$], Mg-amesite [$Si_2Al_4Mg_4O_{10}(OH)_8$] and sudoite [$Si_3Al_4(Mg,Fe)_2\square O_{10}(OH)_8$]. These end members are necessary to model the (i) tschermak (TK), (ii) Fe-Mg (FM), and (iii) dioctahedral-trioctahedral (DT) substitutions in chlorite. Temperatures of chlorite formation in alteration and ore zones (reefs) have been calculated from the equations of state of three intra-crystalline equilibria (eqns. 1 through 3), at a pressure of 2 kbar. The chosen pressure is justified from the fluid inclusion studies discussed below.

$$16daph + 15sud = 20Fe\text{-}am + 6clin + 35qtz + 20H_2O \quad (1)$$

$$2clin + 3Mg\text{-}sud = 4Mg\text{-}am + 7qtz + 4H_2O \quad (2)$$

$$4daph + 6Mg\text{-}sud = 5Fe\text{-}am + 3Mg\text{-}am + 14qtz + 8H_2O \quad (3)$$

Two samples each from the R- and J- reefs were selected for electron microprobe analysis. Representative chlorite analyses, their structural formulae and estimated temperatures are given in Table 1. Average temperatures, estimated using the empirical calibrations fall in the range of 267–301°C. Similarly, average temperatures, computed using reactions (1) through (3) are in the ranges of 268–312°C. Hence, both approaches furnished comparable temperatures, with reasonable standard deviations. However, it should be noted that whenever the estimated temperature values are high, the calculated X_{Fe}^{3+} values are too low. In order to reduce the temperature, a_{H2O} is decreased to as low as 0.2. This is mainly because a decrease of X_{Fe}^{3+} leads to a related decrease of octahedral Al and vacancy with increase in octahedral summation, consequently leading to an increase in the estimated temperature (Vidal et al. 2005; 2006). Similarly a decrease in a_{H2O} leads to a decrease in the equilibrium constants of reactions (1) through (3) and therefore decreases the estimated temperature. A decrease in fluid content in the rock suggest periods of reduced fluid flow due to closure of the fractures during interseismic stage (Sibson, 2001). In the present case, reduced a_{H2O} values were used to make the temperatures compatible with those obtained by empirical calibrations.

Ore mineralogy

In the inner zone, the dominant sulfide minerals are, in decreasing order of abundance, pyrite and arsenopyrite, with minor chalcopyrite, pyrrhotite and galena. In the proximal zone pyrite, arsenopyrite, chalcopyrite, pyrrhotite, and sphalerite occur. Ilmenite, rutile, and titanite occur in both zones. Ore mineral aggregates are aligned along the sheared and mylonitized fabric. Texturally, three types of pyrite and two types of arsenopyrite are present (Figs. 8a and 9). Pyrite-I ranges in size between 100μm and >1mm. It forms porphyroblasts with the shear foliation wrapping around them (Figs. 7g, h, 8a and 9). Euhedral grains of pyrite-I contain numerous randomly to preferentially oriented silicate inclusions mimic matrix foliation (Figs. 7g, h and 8b). Sulfides such as chalcopyrite, pyrrhotite and galena and gold also occur as inclusions (Figs. 8c, d). Pyrite-II, which overgrew pyrite-I, has also euhedral grain boundaries and is almost free of silicate inclusions (Figs. 8a, d) but contains inclusions of other sulfides such as chalcopyrite, arsenopyrite-II and pyrrhotite (Fig.

8d). Pyrite-III has a characteristic irregular outline with or without silicate inclusions and occurs as elongated grains aligned either along the shear foliation or overgrowing this deformation fabric (Fig. 8a). Pyrite-I contains up to 2.8 wt % As and may be referred to as arsenian pyrite (cf. Large et al. 2009). SEM-back scattered electron (BSE) images show that these pyrites are weakly zoned with respect to As showing As-poor cores (Fig. 8e). Pyrite-II shows concentric As-rich and As-poor zones (Figs. 8f, g) but also irregular As zoning patterns (Fig. 8h). Arsenopyrite-I is represented by large euhedral grains with abundant randomly oriented silicate inclusions and may contain inclusions of pyrite-II (Fig. 8b). Arsenopyrite-II is euhedral to subhedral in shape, smaller in size and free of any silicate inclusions (Figs. 8c, d). Arsenopyrite-II in places overgrows pyrite-I (Fig. 8c). Gold occurs mostly in association with sulfides and occasionally as free gold grains in quartz veins. Gold grains are generally 10–20 μm in size and occasionally as large as 100 μm. Gold occurs as

(1) inclusions within pyrite-I, at the interface with other sulfides like chalcopyrite with pyrite (Fig. 10a),

(2) inclusions within pyrite-I without other sulfide inclusions (Fig. 10b),

(3) inclusions within arsenopyrite-II (Fig. 10c), and

(4) free gold in the silicate matrix in close proximity to sulfides and chlorite (Fig. 10d).

Arsenopyrite geothermometry

As described earlier, arsenopyrite- I and II occur in association with pyrite in the proximal and inner alteration zones. The temperature of formation can be inferred from arsenic contents of arsenopyrite as described in Kretschmar and Scott (1976) and Sharp et al. (1985). In selected samples (KU10A and KU16) arsenopyrite grains were analyzed by electron microprobe. Representative analytical data and the deduced temperatures are summarized in Table 2. In sulfur rich assemblage (arsenopyrite with pyrite and/or pyrrhotite) arsenopyrite may contain less than 30 atomic % arsenic due to non-equilibrium feature reflecting the kinetics of growth of arsenopyrite and local fluctuations in f_{S2}/f_{As2} (Kretschmar and Scott 1976). Temperature values were inferred up to ~28.4 atomic % arsenic. The estimated temperatures vary from 255 °C to 318°C, while the corresponding $\log f_{S2}$ falls in the range of –9.9 to –12, comparing well to the temperatures obtained from chlorite geothermometry.

Fluid inclusion studies

Fluid inclusion studies, involving inclusion petrography, microthermometry and Raman spectroscopy in quartz veins from all reefs were carried out. A total of nine doubly polished wafer sections were prepared for examination and five samples (two from R- and J-reefs and one sample from H-reef) were selected for microthermometry. The choice of these samples was based on the availability of workable inclusions within suitable Group of Synchronous Inclusions (GSI, cf. Touret 2001). Grains that showed indications of dynamic recrystallization and inclusions showing stretching or leakage were carefully avoided.

Inclusions are generally small in size ranging from less than 2 µm to 10 µm. Inclusions occurring as isolated, clustered and as intra-granular trails were considered as primary and pseudo secondary, respectively, and selected for microthermometric runs. Inclusions were classified on the basis of disposition and phase content in ambient laboratory conditions, and grouped into four types. Type-I aqueous gaseous inclusions contain a dark gas-rich bubble surrounded by aqueous liquid (Fig. 11a). The volume percent of gaseous phase varies from 40 to 90 % (Table 3). At times inclusion walls are decrepitated due to high internal pressure while heating the inclusions. Type-II and type-III inclusions are monophase gaseous inclusions in which type-II inclusions exclusively contain pure methane as a gas phase (Figs. 11b, c). Type-III inclusions contain a gas mixture of CO_2 and CH_4 with varying proportions (X_{CH4} up to 0.31; Table 3) (Figs. 11b, d). Type-IV inclusions are low salinity aqueous biphase inclusions (Fig. 11e) that frequently occur within the same clusters as type-II and III inclusions (Fig. 11f) and in places they also occur as intra-granular trails. Vapor occupies 10 to 20 % of volume in type-IV inclusions.

For type-I inclusions complete microthermometry data could be obtained on only 21 inclusions (12 from R-reef and 9 from J-reef; Table 3). The temperature of CO_2 melting ($T_{m,CO2}$) varies from -57.8 to -63.2 °C and the temperature of CO_2 vapor homogenization ($T_{h,CO2}$) varies from -15.5 to +7.8 °C. Clathrate melting ($T_{m,Cl}$) varies from +7.8 to +14.8 C. Temperature of total homogenization ($T_{h,tot}$) varies from 272 to 367 °C. For some of the inclusions decrepitation temperatures were recorded and the final homogenization was into a gaseous phase. The temperature of CH_4 vapor homogenization ($T_{h,CH4}$) for type-II inclusions varies from -94.3 to -84.3 °C (Fig.

12a). The temperature of CH_4 melting ($T_{m,CH4}$) could not be measured because the stage only cools to -196 °C using liquid nitrogen as cooling agent. For type-III inclusions the observed variation in $T_{m,CO2}$: was -63.9 to -56.6 °C (Fig.12b). $T_{h,CO2}$ varied from -20.1 to +18.3 °C (Fig.12c). From Raman spectrometric analyses CH_4 (Fig. 11d) is the only gas identified in these inclusions apart from CO_2. For type-IV inclusions temperatures of last ice melting ($T_{m,ice}$) varied from -16.1 to +0.2 °C (Fig. 12d) and final liquid vapor homogenization ($T_{h,tot}$) was into liquid phase with values ranged from 115 to 302 °C (Fig. 12e).

The average calculated salinity for type-IV inclusions is 6.5±4.3 (wt% NaCl equiv.). The isochore intersection geobarometric method described by Roedder and Bodnar (1980) was adopted to estimate the entrapment P-T conditions of the inclusions. Coexisting carbonic (type-III) and aqueous (type-IV) inclusions occurring in the same GSI are considered as coeval inclusions (Fig. 11f). The assumption is that these inclusions were entrapped simultaneously and no post-entrapment modifications of the inclusions had taken place. Two intersection points, from the isochores of these inclusion types, IS-1 (275 °C and 1.8 kbar) and IS-2 (287 °C and 1.5 kbar) furnished P-T values (Fig 13). In addition, pressure values were further inferred from the intersection of the isochores with chlorite (CT) and arsenopyrite (AT) geothermometry (Fig 13). This intersection additionally furnished a pressure range of 1.1 to 2.5 kbar with the thermometry by the two above independent approaches yielding comparable P-T values. This further supports the use of the isochore intersection method.

Re–Os geochronology

Two samples from each of the three mineralized reefs were selected for Re-Os analysis to determine the age of sulfide and gold mineralization. The samples were collected from the fault-fill laminated quartz veins in the inner zone that contains a profuse amount of sulfides in very close association with the gold mineralization. The Re-Os data for the six samples are presented in Table 4. The pyrite and arsenopyrite grains contain between ~0.2 and 4.7 ppb Re and 32 and 240 ppt Os. A significant portion of the Os budget comprises ^{192}Os (7.7 to 45 ppt). The $^{187}Re/^{188}Os$ values are low and range from ~19 to 210. These values positively correlate with the $^{187}Os/^{188}Os$ from ~1.11 to 9.44. Regression of the Re-Os data including rho using isoplot v. 4.15

(Ludwig, 1980) and the ^{187}Re decay (1.666 e^{-11} a^{-1}; Smoliar et al. 1996) yield a Model 1 Re-Os age of 2563 ± 84 Ma (MSWD = 0.38), with a relatively unradiogenic initial $^{187}Os/^{188}Os$ value of 0.29 ± 0.08 (Fig. 14).

Discussion and conclusions

Regional and mine scale structures

Although three regional-scale deformation events (D_1, D_2, and D_3) have been described (Gold and Von Veh 1995 and Gold 2006), only an earlier set of ductile-brittle structures and a final brittle deformation are recognized in the mine. Since mineralization postdates the emplacement of the post-Pongola granites which occurred between D_2 and D_3, the initial development of the shear zone is considered to have developed during D_1 with mineralization occurring during D_3 involving folding and shear zone reactivation. D_1 generated the initial KSZ geometry (R-reef) and footwall splay (H-reef) during NNW-oriented thrusting. The D_2 event, which is regionally related to the emplacement of mafic dykes and sills and which was followed by the emplacement of the post-Pongola granites, is not recognized in the mine as forming any distinct meso- or microscale structures.

The area south-west of Swaziland, where the Mozaan Group is most extensively developed and which includes the Klipwal mine, is characterized by the lowest-grade metamorphic imprint of all the exposed Pongola Supergroup. This region was classified as "unmetamorphosed" by Saggerson and Turner (1995), although it should more appropriately be referred to as "very-low grade metamorphic" with no evidence that regional metamorphism ever exceeded lowermost greenschist facies during any of the deformational events. If the original KSZ formed during D_1, under very-low grade metamorphic conditions, the subsequent reactivation of structures and mineralization during the regional D_3 event occurred under similar temperature conditions, making the two events difficult to distinguish. Nevertheless, microstructural evidence confirms post-D_1 ductile deformation. As sulfide growth generally postdates the early-formed (D_1) shear zone, the sulfides can be used as microstructural markers with respect to ductile overprinting of D_1 structures during D_3. Critical evidence includes the preservation of an early-formed foliation as inclusion trails within sulfides, and sulfide-matrix relationships (strain fringes,

575 foliation wrapping around sulfides, while late-formed sufides overgrew the foliation;
576 Figs. 7g, h, 8a and 9). Thus, the period of sulfide growth overlaps to a large extent
577 with D_3 deformation.

578 The thermobarometric data extracted from the mineralized rocks, as well as
579 the related structures, are considered to represent the metamorphic-structural D_3
580 overprint as supported by the consistency of the data between silicate equilibria and
581 sulfides. Mineralization was related to a substantial influx of fluids during D_3. Fluid
582 pathways exploited the D_3-modified and reactivated KSZ and its related vein systems
583 as well as lithological contacts, becoming sites of sulfide-gold precipitation. The
584 actual origin of the mineralizing fluid remains to be discussed, but late fluid
585 infiltration can be recognized on a regional scale. Saggerson and Turner (1995) note
586 that post-peak hydrous alteration of metamorphic mineral assemblages is widespread
587 in the Pongola Supergroup. The final (post-D_3) brittle effects on the shear zone
588 produced fault breccia comprising fragments of quartz veins, mineralized domains
589 and mylonitic wall rocks (Fig. 4d). This event is most likely part of the regional Karoo
590 extensional faulting related to the breakup of Gondwana.

591 The J-reef with higher gold grades was developed at the contact between
592 metapsammite and chlorite-carbonate schist (Figs. 2a and 5). Hence the original
593 lithological discontinuity provided a fluid conduit for J-reef mineralization. On the
594 regional scale, the KSZ strikes approximately N–S. However, at the KGM there is a
595 change in direction from the N–S to a NNE–SSW orientation (Fig.1c). This change in
596 the shear zone geometry, is considered to be a result of the regional D_3 folding event
597 which produced a convex westward flexure in the KSZ and generated a
598 'compressional jog' through which regional fluid flow was driven (cf. Cox et al. 2001;
599 Sibson, 2001).

600 The shear zone contains profuse laminated quartz veins that are developed as
601 fault-fill veins (Fig 4a) due to formation of microfractures along the shear planes.
602 Microfracturing, along grain boundaries, is the dominant mechanism for the formation
603 of grain scale porosities in the ductile regime (Knipe and McCaig 1994; McCaig
604 1997; Mancktelow et al. 1998; Kolb et al. 2004). These microfractures generate
605 fracture porosity and increase fluid permeability along the shear zone (Cox et al.
606 2001), increasing pervasive fluid flow through the shear zone. Fractures provided the
607 open space for rapid flow of the gold-bearing ore fluids. The 'jigsaw-puzzle' type
608 brittle fracturing with angular fragments observed in sulfide grains (Fig. 8f) are

interpreted to represent hydraulic breccias which point to hydraulic fracturing, as a mechanism for fracture formation, as described by Robert et al. (1995); Kisters et al. (2000) and Kolb et al. (2004).

Extensional veins and pressure fluctuation

Oblique or sub-horizontal extensional vein arrays are also observed in association with the shear zone and fault-fill veins (Fig. 4c). These veins represent hydraulic extension fractures, which opened during vein filling episodes by fluid pressures (P_f) in excess of the lithostatic pressure (i.e., $P_f \geq \sigma_3 + T$, where T = tensile strength of the rock) (Robert and Brown 1986). Extensional fractures typically develop parallel to σ_1 when σ_3' ($\sigma_3' = \sigma_3 - P_f$) equals or exceeds the tensile strength of the rock. This situation is only possible under conditions of low differential stress. Hence, extensional fracturing (possible at negative values of σ_3') can only be attainable by elevated fluid pressure in the inferred compressional environments of formation of orogenic gold deposits (Sibson et al. 1988; Sibson 2001; Robert and Poulsen 2001).

Kolb et al. (2004) demonstrated the effect of change in shear zone geometry for economic gold mineralization in the world class Hutti gold mine in the Hutti-Muski greenstone belt, eastern Dharwar craton, India. Mishra and Pal (2008) reported oblique sigmoidal extensional veins, similar to the subhorizontal extensional veins in the KSZ in the Hira-Buddini mine from the same Hutti-Muski greenstone belt. These veins were formed by hydraulic fracturing during brittle-ductile shearing. At the Val d'Or lode gold deposits at Quebec Canada, Bouillier and Robert (1992) established that successive cycles of opening and collapse in subhorizontal extension veins correlated with opening and slip on high-angle shear veins. They interpreted these observations to be a result of fluid pressure fluctuations in successive coseismic-interseismic cycles (McCuig and Kerrich 1998). Formation of laminated quartz veins requires episodes in which fluid pressure exceeds the local normal stress on the fault. Hence, a crack-seal and/or a fault valve mechanism are interpreted to have operated at KGM during the mineralization event producing the laminated veins.

Fluid inclusion density variation further supports pressure fluctuation during gold mineralization. The wide distribution in $T_{h,CO2}$ values of Type-III inclusions indicates a significant variation in density (Table 3), which is attributed to fluctuation in fluid composition and/or pressure. In order to determine the exclusive effect of

pressure, $T_{m,CO2}$–$T_{h,CO2}$ plots (Fig. 12f) were prepared for inclusions with maximum lowering in $T_{m,CO2}$ up to −57 °C, i.e., pure CO_2. The plot shows significant variation of $T_{h,CO2}$ for a near-constant $T_{m,CO2}$, implying fluid pressure fluctuations at the time of entrapment (cf. Dugdale and Hagemann, 2001).

Crystal plastic deformation microstructures are observed in the quartz grains but are absent in feldspar grains, which suggests that the deformation occurred at greenschist facies conditions (Scholz, 1988). Dynamic recrystallization structures of quartz grains shows bulged and recrystallized grain boundaries, subgrain rotation and core-mantle structures indicative of pressure solution and intracrystalline plastic deformation at temperatures of about 300°C (Stipp et al. 2002). The alteration mineral assemblage consisting of chlorite-muscovite-carbonates±epidote-quartz-pyrite-arsenopyrite surrounding the shear zone in the host rocks is characteristic of low to sub-greenschist facies conditions. Estimates from fluid inclusion isochore intersections coupled with the chlorite and arsenopyrite thermometry (Fig. 13) further confirm that the P-T conditions (255–318°C and 1.1 to 2.5 kbar) were at sub-greenschist facies. These temperatures and the observed alteration mineralogy in the proximal and inner zone are consistent with the typical mesozonal orogenic gold deposits elsewhere (McCuaig and Kerrich 1998; Groves et al. 1998; Goldfarb et al. 2001; Groves et al. 2003; Elmer et al. 2006).

Ore fluid composition

Irrespective of the host rock, metamorphism and age, the observed fluid composition in orogenic gold deposits shows a very narrow range which is in general aqueous-gaseous, low saline metamorphic and/or distant magmatic (Mikcuki 1998; McCuiag and Kerrich 1998). For the Klipwal deposit, fluid inclusion studies reveal that the original mineralizing fluid composition is H_2O-CO_2-CH_4-low salinity (~6 wt.% NaCl equiv.). This is comparable with orogenic gold deposits around the world (Table 5) in general, and sedimentary rock-hosted, Phanerozoic counter-parts in the Pacific Rim (North American Cordellera, Paleozoic-Mesozoic orogenic belts in Asia and in eastern New Zealand) in particular (Bierlein and Crowe 2000).

Mechanisms of mineralization

At Klipwal, gold mineralization is localized in a brittle-ductile, oblique-reverse, sinistral shear zone and associated fault splays. Gold is confined to laminated quartz veins within the sheared host rocks and also occurs in the alteration halo. It is postulated that the initial, auriferous, sulfur-rich, low salinity H_2O-CO_2-CH_4 fluid was transported to near-surface levels via a deep-rooted brittle-ductile shear zone, located at the contact of contrasting lithologic units and at a westward flexure of the KSZ, which acted as the favorable site for high-volume fluid flow. Pressure cycling (Robert et al. 1995) or the fault-valve mechanism (Sibson et al. 1988; Sibson 2001) is indicated by the presence of coexisting aqueous and carbonic inclusions that show wide variations in density (Fig. 12f). Although P-T values obtained by inclusion thermobarometry coupled with chlorite and arsenopyrite geothermometry (1.1 to 2.5 kbar and 265 to 315°C) are comparable with the P-T window of the orogenic gold deposits (Table 5), there is convincing evidence of near-isothermal pressure fluctuation (about 1.4 kbar). Pressure fluctuation facilitated phase separation of gaseous and aqueous fluid (Wilkinson and Johnston, 1996; Mikucki, 1998) resulting in a decrease in total sulfur content of the ore fluid, and leading to precipitation of free gold in quartz veins along with chlorite. Fluid-wall rock interaction, on the other hand, was responsible for the association of gold with sulfides where a decrease in fO_2 occurred (cf. Mikucki 1998). The presence of type-II pure CH_4 bearing inclusions and type-III CH_4-rich inclusions in close association with CO_2-rich carbonic inclusions is evidence for a decrease or fluctuation in ambient fO_2 conditions.

Timing of mineralization and source of ore fluid

The relative timing of mineralization is important for identifying the source of ore fluid and gold. Two possible models have been proposed for the source of gold-bearing hydrothermal fluid. These include (1) prograde metamorphic devolatilization of host rocks; (2) magmatic fluid originating from extensive regional or specific granitic intrusions (Hagemann and Cassidy 2000 and references therein; Tomkins 2013). Archaean orogenic lode gold mineralization, in general, is formed at a late stage in the tectono-magmatic evolution of the host terrane. Most of these gold-quartz lode veins are formed after peak metamorphism of the immediately surrounding host rocks, in greenschist facies deposits (Groves et al. 1998; Ridley and Diamond 2000; Goldfarb et al. 2001; Groves et al. 2003).

At Klipwal, the pyrite and arsenopyrite Re-Os data provide the timing of gold mineralization at 2563±84 Ma. The initial Os isotope composition ($^{187}Os/^{188}Os_i$) from these sulfide grains can be used to infer the source of sulfides and by inference ore fluid and gold. In general, the mantle has relatively low amounts of Re, when compared with crustal rocks, with respect to Os concentration (Kirk et al. 2002). This is because crustal rocks are the products of partial melting of the mantle and potentially re-melted products of previously formed crust. During partial melting Re partitions more readily into the melt and as a result crustal rocks have higher Re/Os values and thus rapidly evolve to develop elevated $^{187}Os/^{188}Os$ ratios (Kirk et al. 2002; Kirk et al. 2003). The low non-radiogenic initial $^{187}Os/^{188}Os_i$ (0.29 ± 0.08) value determined from the Re-Os data (Fig. 14) suggests that the sulfides and, by inference, gold were originally derived from more primitive sources (cf. Reisberg et al 1991; Selby 2007; Moreli et al. 2007), the most likely being mafic volcanic rocks in the underlying Nsuze Group or mafic-ultramafic greenstone belts, such as the Nodweni greenstone belt, which released non-radiogenic Os.

The post-Pongola granitic intrusions (between 2863 and 2721 Ma) had been considered as a potential source of the ore fluid for the Klipwal mineralization. However, fluid inclusion studies provided no evidence of magmatic fluid components and Re-Os sulfide geochronology, even with the large error attached to the age date (2563±84 Ma) shows that mineralization is much younger than the post-Pongola granitic intrusions. Hence, there is no basis for relating these granites to gold mineralization.

Instead, we propose that devolatilization during metamorphism of the Pongola volcano-sedimentary sequence and perhaps deeper-seated greenstones of the Kaapvaal basement, previously metamorphosed at sub-greenschist to greenschist facies conditions, generated the required amounts of fluid. At sufficiently deep levels, a second phase of metamorphism at higher temperatures would cause dehydration of these rocks, with fluids migrating upwards and overprinting successively higher-level rocks, whatever their original metamorphic grade. These fluids may have mixed with mantle components or interacted with mafic to ultramafic rocks at depth, carrying metals to shallow crustal levels with fluid flow locally focused into the Klipwal shear zone, precipitating gold-quartz and carbonate veins.

Acknowledgements

SSC acknowledges the University of KwaZulu-Natal for providing the post-doctoral scholarship. The Department of Geology & Geophysics, IIT Kharagpur, India is acknowledged for providing SEM-BSE and reflected-light photomicrography facilities. The cooperation and help extended by the mine management at Klipwal Gold Mine is gratefully acknowledged. An anonymous reviewer, Dr. Lynnette Greyling and associate editor Dr. Hartwig Frimmel are thanked for their constructive comments and suggestions that greatly helped to improve the quality of the manuscript. The editor Dr. Bernd Lehmann is thanked for editorial handling. Comments from Dr. Jochen Kolb on the earlier version of this manuscript are gratefully acknowledged.

References

Armstrong NV, Hunter DR, Wilson AH (1982) Stratigraphy and petrology of the Archaean Nsuze Group, northern Natal and southeastern Transvaal, South Africa. Precamb Res 19:75–107

Bailey SW (1988) Chlorites: structures and crystal chemistry. In Bailey SW (ed) Hydrous Phyllosilicates. Rev Mineral 19:347–403

Bakker RJ (1997) CLATHRATES: Computer programs to calculate fluid inclusion V-X properties using clathrate melting temperatures. Computers & Geosciences 23, 1-18

Bakker RJ (1999) Adaptation of the Bowers and Helgeson (1983) equation of state to the H_2O-CO_2-CH_4-N_2-NaCl system. Chem Geol 154:225–236

Bakker RJ (2003) Package FLUIDS 1. Computer programs for analysis of fluid inclusion data and modeling bulk fluid properties. Chem Geol 194: 3–23

Barnicoat AC, Henderson IHC, Knipe RJ, Yardley BWD, Napier RW, Fox NPC, Kenyen AK, Muntingh DJ, Strydom D, Winkler KS, Lawrence SR, Cornford C (1997) Hydrothermal gold mineralization in the Witwatersrand basin. Nature 386:820–824

Barton JM, Hunter DR, Jackson MPA, Wilson AC (1983) Geochronologic and Sr-isotopic studies of certain units in the Barberton granite-greenstone terrain, Swaziland. Transactions Geol Soc South Afr 86:71–80

778 Belonoshko AB, Saxena SK (1991) A molecular dynamics study of the pressure-
779 volume-temperature properties of super-critical fluids:II. CO_2,CH_4,CO,O_2 and H_2.
780 Geochm Cosmochim Acta 55:3191–3208
781 Bierlein FP, Crowe DE (2000) Phanerozoic orogenic lode gold deposits: Rev Econ
782 Geol 13:103–139
783 Bodnar RJ (1993) Revised equation and table for determining the freezing point
784 depression of H2O-NaCl solutions. Geochim. Cosmochim. Acta 57:683–684
785 Boulllier AM, Robert F (1992) Palaeoseismic events recorded in Abinbi gold-quartz
786 vein networks, Val d'or, Abitibi, Quebec,Canada. J Struct Geol 14:161–179
787 Bullen WD, Thomas RJ, McKenzie A (1994) Gold mineralization in Natal, South
788 Africa. J Afr Earth Sci 18: 99–109
789 Burke EAJ (2001) Raman microspectrometry of fluid inclusions. Lithos 55: 39–158
790 Cathelineau M, Nieva D (1985) A chlorite solid solution geothermometer The Los
791 Azufres (Mexico) geothermal system. Contrib Mineral Petrol 91:235–244
792 Chinnasamy SS, Mishra B (2013) Greenstone metamorphism, hydrothermal alteration
793 and gold mineralization in the genetic context of the granodiorite-hosted gold
794 deposit at Jonnagiri, eastern Dharwar craton, India. Econ Geol 108:1015–1036
795 Cooper RA, Tulloch AJ (1992) Early Palaeozoic terranes in New Zealand and their
796 relationship to the Lachlan fold belt. Tectonophysics 214:129–144
797 Cox SF, Knackstedt MA, Braun J (2001) Principles of structural control on
798 permeability and fluid flow in hydrothermal systems. In: Richards JP, Tosdal RM
799 (eds) Structural Controls on Ore Genesis. Rev Econ Geol 14:1 –24
800 Cumming VM, Poulton SW, Rooney AD, Selby D (2013) Anoxia in the terrestrial
801 environment during the late Mesoproterozoic. Geology 41:583–586
802 Cumming VM, Selby D, Lillis PG (2012) Re-Os geochronology of the lacustrine
803 Green River Formation: Insights into direct dating of lacustrine successions, Re-
804 Os systematics and paleocontinental weathering. Earth Planet Sci Lett 359:194–
805 205
806 de Ronde CEJ, Spooner ETC, de Wit MJ, Bray CJ (1992) Shear zone-related, Au
807 quartz vein deposits in the Barberton greenstone belt, South Africa: field and
808 petrographic characteristics, fluid properties, and light stable isotope
809 geochemistry. Econ Geol 87:366-402
810 Duan Z, Møller N, Weare JH (1992a) Molecular dynamics simulation of PVT
811 properties of geological fluids and a general equation of state of nonpolar and

812 weakly polar gases up to 2000 K and 20,000 bar. Geochim Cosmochim Acta
813 56:3839–3845
814 Duan Z, Møller N, Weare JH (1992b) An equation of state for the CH_4-CO_2-H_2O
815 system: I. Pure systems from 0 to 1000°C and 0 to 8000 bar. Geochim
816 Cosmochim Acta 56:2605–2617
817 Duan Z, Møller N, Weare JH (1992c). An equation of state for the CH_4-CO_2-H_2O
818 system: II. Mixtures from 50 to 1000°C and 0 to 1000 bar. Geochim Cosmochim
819 Acta 56:2619–2631
820 Dugdale AL, Hagemann SG (2001) The Bronzewing lode-gold deposit, Western
821 Australia: P-T-X evidence for fluid immiscibility caused by cyclic decompression
822 in gold-bearing quartz veins. Chem Geol 173:59–90
823 Elmer FL, White RW, Powell R (2006) Devolatilization of metabasic rocks during
824 greenschist-amphibolite facies metamorphism J Metamor Geol 24:497–513
825 Fairmaid AM, Kendrick MA, Phillips D, Fu B (2011) The origin and evolution of
826 mineralizing fluids in a sediment-hosted orogenic-gold deposit, Ballarat East,
827 Southeastern Australia. Econ Geol 106: 653–666
828 Farrow DJ, Harmer RE, Hunter DR, Eglington BM (1990) Rb-Sr and Pb-Pb dating of
829 the Anhalt leuco-tonalite, northern Natal. South Afr J Geol 93:696–701
830 Frimmel HE, Gartz VH (1997) Witwatersrand gold particle chemistry matches model
831 of metamorphosed, hydrothermally altered placer deposits: Mineral Deposit
832 32:523–530
833 Frimmel HE, Hallbauer DK, Gartz VH (1999) Gold mobilizing fluids in the
834 Witwatersrand Basin: composition and possible sources. Mineral Petrol 66:55– 81
835 Gao ZL, Kwak TAP (1995a) Turbidite-hosted gold deposits in the Bendgo-Ballart and
836 Melbourne zones, Australia I: Geology, mineralization. Stable isotopes and
837 implications for exploration. Int Geol Rev 37: 910–944
838 Gao ZL, Kwak TAP (1995b) Turbidite-hosted gold deposits in the Bendgo-Ballart
839 and Melbourne zones, Australia II: Nature of ore fluids. Int Geol Rev 37:1007–
840 1038
841 Gold DJC (1993) The geological evolution of a part of the Pongola basin,
842 southeastern Kaapvaal craton. Unpublished Ph.D. Thesis. University Natal,
843 Pietermaritzburg, South Africa. pp 156

844 Gold DJC (2006) The Pongola Supergroup. In: Johnson MR, Anhaeusser CR, Thomas
845 RJ (eds) The Geology of South Africa. Geol Soc South Afr, Johannesburg,
846 Council for Geoscience 135–148
847 Gold DJC, Von Veh MW (1995) Tectonic evolution of the Late Archaean Pongola-
848 Mozaan basin, South Africa. J Afr Earth Sci 21:203–212
849 Goldfarb RJ, Baker T, Dube B, Groves DI, Hart CJR, Gosselin P (2005) Distribution,
850 character, and genesis of gold deposits in metamorphic terranes.In: Hedenquist
851 JW, Thompson JFH, Goldfarb RJ, Richards JP (eds) Economic Geology. 100th
852 Anniversary Volume 1905–2005. Littleton, Colorado, Society of Economic
853 Geologists 407–450
854 Goldfarb RJ, Christie T, Skinner D, Haeussler P, Bradley D (1995) Gold deposits of
855 Westland, New Zealand and southern Alaska. Products of the same tectonic
856 processes? In: Mauk J (ed) PACRIM '95. Symp 239–244
857 Goldfarb RJ, Groves DI, Gardoll S (2001) Rotund versus skinny orogens: well-
858 nourished or malnourished gold? Geology 29:539–542
859 Goldfarb RJ, Phillips GN, Nokleberg WJ (1998) Tectonic setting of synorogenic gold
860 deposits of the Pacific Rim. Ore Geol Rev 13:85–218
861 Goldfarb RJ, Snee LW, Miller LD, Newberry RJ (1991) Rapid dewatering of the crust
862 deduced from ages of mesothermal gold deposits. Nature 354:296–298
863 Goldfarb RJ, Snee LW, Pickthorn WJ (1993) Orogenesis, high-*T* thermal events, and
864 gold vein formation within metamorphic rocks of the Alaskan Cordillera. Mineral
865 Mag 57: 375–394
866 Groves DI, Goldfarb RJ, Robert F, Hart CJR (2003) Gold Deposits in Metamorphic
867 Belts: Overview of Current Understanding, Outstanding Problems, Future
868 Research, and Exploration Significance. Econ Geol 99:1–29
869 Groves DI. Goldfarb RJ, Gebre-Mariam M, Hagemann SG, Robert F (1998) Orogenic
870 gold deposits: a proposed classification in the context of their crustal distribution
871 and relationship to other gold deposit types. Ore Geol Rev 13:7–27
872 Hagemann SG, Bray C, Brown PE, Spooner ETC (1996) Combined gas and ion
873 chromatography of fluid inclusions and sulfides from the Archean epizonal
874 Wilualode gold deposits, Western Australia. In: Brown PE, Hegemann SG (eds)
875 Pan-American conference on research on fluid inclusions 6: Program and abstract:
876 Wisconsin, Department of Geology and Geophysics, University of Wisconsin-
877 Madison, 56–58

878 Hagemann SG, Brown PE (1996) Geobarometry in Archean lode gold deposits: Eur J
879 Mineral 8:937–960
880 Hagemann SG, Brown PE (2000) Gold in 2000: An Introduction. Rev Econ Geol 13:
881 1–7
882 Hagemann SG, Cassidy KF (2000) Archaean orogenic lode gold deposits: Rev Econ
883 Geol 13:9–68
884 Hagemann SG, Gebre-Mariam M, Groves DI (1994) Surface-water influx in shallow-
885 level Archean lode gold deposits in Western Australia, Geology 22:1067–1070
886 Hallbaner DK, Utter T (1977) Geochemical and morphological characteristics of gold
887 particles from recent river deposits and the fossil placers of the Witwatersrand.
888 Miner Depos 12: 293–306
889 Hartwig E, Frimmel HE (2002) Genesis of the World's Largest Gold Deposits.
890 Science 297:1815–1817
891 Hegner E, Kröner A, Hofmann AW (1984) Age and isotopic geochemistry of
892 Archaean Pongola and Usushwana suites in Swaziland, southern Africa: a case for
893 crustal contamination of mantle-derived magma. Earth Planet Sci Lett 70:267–279
894 Hegner E, Kröner A, Hofmann AW (1993) Trace element and isotopic constrains on
895 the origin of the Archaean Pongola and Usushwana Igneous Suites in Swaziland.
896 In: Maphalala R, Mabuza m (Compliers), Extended Abstract: 16th International
897 Colloquium on African Geology, Geological Survey and Mines Department,
898 Swaziland pp 147–149
899 Hilliard P (2007) A structural evaluation of the Kilpwal Gold Mine, Unpublished
900 Mine Report, Bosveld Mines (Pty) Ltd pp 15
901 Ho SE (1987) Fluid inclusions: Their potential as an exploration toll for Archean gold
902 deposits. In: Ho SE, Groves DI (eds) Recent advances in understanding
903 Precambrian gold deposits: Geology Department and University Extension,
904 University of Western Australia, Publication No 11:239–263
905 Ho SE, Bennett JM, Cassydy KF, Hronsky JMA, Mikucki EJ, Sang JH (1990) Nature
906 of ore fluid, and transportational and depositional conditions in sub-amphibolite
907 facies deposits In: Ho SE, Groves DI, Bennett JM (eds) Gold deposits of the
908 Archean Yilgarn Block, Western Australia: Nature, genesis and exploration
909 guides: Geology Department (Key Centre) and University Extension, University
910 of Western Australia, Publication no 20:198-211

911 Holland TJB, Baker J, Powell R (1998) Mixing properties and activity-composition
912 relationship of chlorite in the system MgO-FeO-Al_2O_3-SiO_2-H_2O. Eur J Mineral
913 10:395–406
914 Horvath P, Reinhardt J, Hofmann A (2014) High-grade metamorphism of ironstones
915 in the Mesoarchaean of southwest Swaziland. Mineral Petrol 108:589-605
916 Hunter DR, Smith RG, Sleigh DWW (1992) Geochemical studies of Archaean
917 granitoid rocks in the Southeastern Kaapvaal Province: Implications for crustal
918 development J Afr Earth Sci 15:127–151
919 Jacobs GK, Kerrick DM (1980) Methane: An equation of state with application to the
920 ternary system H_2O-CO_2-CH_4, Geochim Cosmochim Acta 45:607–614
921 Kamo SL, Davis DW (1994) Reassessment of Archean crustal development in the
922 Barberton Mountain Land, South Africa, based on U-Pb dating Tectonics 13:167–
923 192
924 Kerrich R, Cassidy KF (1994) Temporal relationships of lode gold mineralization to
925 accretion, magmatism, metamorphism and deformation, Archaean to present: A
926 review. Ore Geol Rev 9:263–310
927 Kirk J, Ruiz J, Chesley J, Titley S (2003) The Origin of Gold in South Africa.
928 American Scientist 91:534–541
929 Kirk J, Ruiz J, Chesley J, Titley S, Walshe J (2001) A detrital model for the origin of
930 gold and sulfides in the Witwatersrand basin based on Re–Os isotopes. Geochim
931 Cosmochim Acta 65:2149–2159
932 Kirk J, Ruiz J, Chesley J, Walshe J, England G (2002) A major Archean gold and
933 crust-forming event in the Kaapvaal Craton, South Africa. Science 297:1856–
934 1858
935 Kisters AFM, Kolb J, Meyer FM, Hoernes S, (2000) Hydrologic segmentation of
936 high-temperature shear zones: structural, geochemical and isotopic constraints
937 from auriferous mylonitesof the Renco Mine, southern Zimbabwe. J Struct Geol
938 22:811 –829
939 Knipe RJ, McCaig AM (1994) Microstructural and microchemical consequences of
940 fluid flow in deforming rocks. In: Parnell J (ed) Geofluids: Origin, Migration and
941 Evolution of Fluid in Sedimentary Basins. Geol Soc Special Publication pp 99–
942 112

943 Kolb J, Rogers A, Meyer F M, Vennemann TW (2004) Development of fluid
944 conduits in the auriferous shear zones of the Hutti Gold Mine, India: evidence for
945 spatially and temporally heterogeneous fluid flow. Tectonophysics 378:65– 84
946 Kretschmar U, Scott SD (1976) Phase relations involving arsenopyrite in the system
947 Fe-As-S and their application. Can Mineral 14:364–386
948 Kretz R (1983) Symbols for rock-forming minerals. Am Mineral 68:277–279
949 Krienitz M-S, Trumbull RB, Hellmann A, Kolb J, Meyer FM, Wiedenbeck M (2008)
950 Hydrothermal gold mineralization at the Hira Buddini gold mine, India: Constraints
951 on fluid evolution and fluid sources from boron isotopic compositions of tourmaline.
952 Miner Depos 43:421–434
953 Lawley C, Selby D, Imber J (2013) Re-Os Molybdenite, Pyrite, and Chalcopyrite
954 Geochronology, Lupa Goldfield, Southwestern Tanzania: Tracing Metallogenic
955 Time Scales at Midcrustal Shear Zones Hosting Orogenic Au Deposits. Econ Geol
956 108:1591–1613
957 Layer PW. Kröner A, McWilliams M, Burghele A (1988) Paleomagnetism and age of
958 the Archean Usushwana Complex, southern Africa. J of Geophy Res 93:449–457
959 Ludwig K R (1980) Calculation of uncertainties of U-Pb isotope data. Earth Plan Sci
960 Let, 46:212–220
961 Mancktelow NS, Grujic D, Johnson EL (1998) An SEM study of porosity and grain
962 boundary microstructure in quartz mylonites, Simplon Fault Zone, Central Alps.
963 Contrib Mineral Petrol 131:71–85
964 Maphalala R, Kröner A (1993) Pb-Pb single zircon ages for the younger Archaean
965 granitoids of Swaziland, southern Africa. In: Maphalala R Mabuz M (eds)
966 Extended Abstracts 16th Colloquium of African Geology.
967 Matthews PE (1990) A plate tectonic model for the Late Archaean Pongola
968 Supergroup in southeastern Africa. In: Sychanthavong SPH (ed), Crustal
969 Evolution and Orogeny. Oxford and IBH Publishing New Delhi pp 41–73
970 Matthews PE, Chatlesworth G, Eglington BM, Harmer RE (1989) A minimum 3.29
971 Ga age for the Nondweni greenstone complex in the south-eastern Kaapvaal
972 Craton. South Afr J Geol 92:272–278
973 McCaig AM (1997) The geochemistry of volatile fluid flow in shear zones. In:
974 Holness, MB (ed) Deformation Enhanced Fluid Transport in the Earth's Crust and
975 Mantle. Mineral Soc Series London pp 227–266

McCuaig TC, Kerrich R (1998) P-T-t-deformation-fluid characteristics of lode gold deposits: evidence from alteration systematics. Ore Geol Rev 12:381–453

Mernagh TP (1996) Gold mineralization at Mount Charlotte: Evidence for fluid oxidation from fluid inclusions: Geol Soc Australia, Abstracts 41 p 292

Mikucki EJ (1998) Hydrothermal transport and depositional processes in Archean lode-gold systems: A review. Ore Geol Rev 13:307–321

Mikucki EJ (1998) Hydrothermal transport and depositional processes in Archean lode-gold systems: A review. Ore Geol Rev 13:307-321

Mikucki EJ, Ridley JR (1993) The hydrothermal fluid of Archaean lode-gold deposits at different metamorphic grades: compositional constraints from ore and wall rock alteration assemblages. Miner Depos 28:469–481

Miller LD, Goldfarb RJ, Snee LW, Gent CA, Krikham RA (1995) Structural geology, age, and mechanisms of gold vein formation at the Kensington and Julian deposits, Berners Bay district, southeast Alaska. Econ Geol 90:343–368

Minter WEL (1999) Irrefutable detrital origin of Witwatersrand gold and evidence of aeolian signatures: Econ Geol 94:665–670

Mishra B, Pal N (2008) Metamorphism, Fluid Flux, and Fluid Evolution Relative to Gold Mineralization in the Hutti-Maski Greenstone Belt, Eastern Dharwar Craton, India Econ Geol 103:801–827

Mishra B, Panigrahi MK (1999) Fluid evolution in the Kolar gold field: evidence from fluid inclusion studies. Miner Depos 34:173-181

Morelli R, Creaser RA, Seltmann R, Stuart FM, Selby D, Graupner T (2007) Age and source constraints for the giant Muruntau gold deposit, Uzbekistan, from coupled Re-Os-He isotopes in arsenopyrite. Geology 35:795–798

Mueller AG, Groves DI (1991) The classification of Western Australian greenstone-hosted gold deposits according to wall rock alteration mineral assemblages. Ore Geol Rev 6:291-331

Mukasa SB, Wilson AH, Young KR (2013) Geochronological constraints on the magmatic and tectonic development of the Pongola Supergroup (Central Region), South Africa. Precamb Res 224:268–286

Nokleberg WJ, Bundtzen TK, Dawson KM et al (1996) Significant metalliferous lode deposits and placer districts for the Russian Far East, Alaska and the Canadian Cordillera: United States Geological Survey Open-File report 96-513-A p 385

1009 Nokleberg WJ, Plafker G, Wilson FH (1994) Geology of south-central Alaska. In:
1010 Plafker G Berg HC (eds) The Geology of Alaska. Geol. Soc. Am G-1 pp. 311–366
1011 Pal N, Mishra B (2002) Alteration geochemistry and fluid inclusion characteristics of
1012 the greenstone hosted gold deposit at Hutti, Eastern Dharwar Craton, India. Miner
1013 Depos 37:722–736
1014 Peters SG, Golding SD, Dowling K (1990) Melange- and sediment-hosted gold-
1015 bearing quartz veins, Hodgkinson gold field, Queensland, Australia. Econ Geol
1016 85:312–327
1017 Phillips GN, Hughes MJ (1996) The geology and gold deposits of the Victorian gold
1018 province. Ore Geol Rev 11:255–302
1019 Phillips GN, Law JDM (2000) Witwatersrand gold fields: geology, genesis and
1020 exploration. Rev Econ Geol 13:439–500
1021 Pouchou JL Pichoir F (1984) A new model for quantitative X-ray microanalyses, Part
1022 I: application to the analyses of homogenous samples. Recherche Aerospatiale,
1023 3:13–36
1024 Pretorius DA (1981) Gold and uranium in quartz-pebble conglomerates. Econ Geol
1025 75th Anniversary Volume pp 117–138
1026 Ramsay WRH, Bierlein FP, Arne DC, Vandenberg AHM (1998) A review of
1027 turbidite-hosted gold deposites central Victoria: regional setting, styles of
1028 mineralluzation and genetic constrains Ore Geol Rev 13:131–151
1029 Reimold WU, Meyer FM, Walraven F, Matthews PE (1993) Geochemistry and
1030 chronology of Pre- and post-Pongola granitoids from northeastern Natal. In:
1031 Maphalala R, Mabuza M (eds) Extended Abstracts from the 16th Colloquium on
1032 African Geology, Geol Survey Mbabane Swaziland. 294–296
1033 Reisberg LC, Allrgre CJ, Luck J-M (1991) The Re-Os systematics of the Ronda
1034 Ultramafic Complex of southern Spain Earth Planet Sci Lett 105: 196–213
1035 Ridley JR, Diamond LW (2000) Fluid chemistry of orogenic lode gold deposits and
1036 implications for genetic models. Rev Econ Geol 13:141–162
1037 Robb LJ, Brandl G, Anhaeusser CR, Poujol M (2006) Archaean granitoid intrusions
1038 of the Kaapvaal Craton. In: Johnson MR, Anhaeusser CR, Thomas RJ (eds) The
1039 Geology of South Africa. Geol Soc South Afr Council for Geoscience pp 57–94
1040 Robb LJ, Meyer FM (1995) The Witwatersrand Basin, South Africa: Geological
1041 framework and mineralization processes. Ore Geol Rev 10:67–94

1042 Robert F, Boullier AM, Firdaous K (1995). Gold–quartz veins in metamorphic
1043 terranes and their bearing on the role of fluids in faulting. J Geophy Res
1044 100:12861–12879
1045 Robert F, Brown AC (1986) Archaean gold-bearing quartz veins at the Sigma mine,
1046 Abitibi greenstone belt, Quebec. Part I. Geologic relations and formations of the
1047 vein systems. Econ Geol 81:578–592
1048 Robert F, Kelly WC (1987) Ore forming fluids in Archaean gold-bearing quartz veins
1049 at the Sigma Mine, Abitibi greenstone belt, Quebec, Canada. Econ Geol 82:1464-
1050 1482
1051 Robert F, Poulsen KH (2001) Vein fomation and deformation in greenstone gold
1052 deposits. In: Richards JP, Tosdal RM (eds) Structural control on ore genesis. Rev
1053 Econ Geol 14:111-155
1054 Roedder E, Bodnar RJ (1980) Geologic pressure determination from fluid inclusion
1055 studies. Ann Rev Earth Plan Sci 8:263–301
1056 Roering C (1968) The tectonics of the West Rand Syncline: A field study of brittle
1057 failure in the Witwatersrand Basin, Econ Geol Unit Univ. Witwatersrand
1058 Johannesburg Inform Circ 48: pp 28
1059 Saggerson EP, Turner, LM (1995) A Review of Metamorphism in the Republic of
1060 South Africa and the Kingdoms of Lesotho and Swaziland. Explanation of
1061 Metamorphic Map 1: 1 000 000. Council for Geoscience, Pretoria, 285 pp.
1062 Saravanan CS, Mishra B, Jairam MS (2009) P-T conditions of mineralization in the
1063 Jonnagiri granitoid-hosted gold deposit, eastern Dharwar craton, southern India:
1064 Constraints from fluid inclusions and chlorite thermometry. Ore Geol Rev
1065 36:333–349
1066 Scholz CH (1988) The brittle-plastic transition and the depth of seismic faulting.
1067 Geologische Rundschau 77:319–328
1068 Selby D (2007) Direct rhenium-osmium age of the Oxfordian-Kimmeridgian
1069 boundary, Staffin bay, Isle of Skye, UK and the Late Jurassic time scale.
1070 Norwegian Jour Geol 87:291–299
1071 Selby D, Kelley KD, Hitzman MW, Zieg J (2009) Re-Os sulfide (bornite,
1072 chalcopyrite, and pyrite) systematics of the carbonate-hosted copper deposits at
1073 Ruby Creek, southern Brooks Range, Alaska. Econ Geol 104:437–444

1074 Sharp ZD, Essene, EJ, Kelly, WC (1985) A reexamination of the arsenopyrite
1075 geothermometer: pressure considerations and applications to natural assemblages.
1076 Can Mineral 23:517–534
1077 Sibson RH, Robert F, Poulsen H (1988) High angle faults, fluid pressure cycling and
1078 mesothermal gold-quartz deposits. Geology 16:551–555
1079 Sibson, RH (2001) Seismogenic framework for hydrothermal transport and ore
1080 deposition. In: Richards JP, Tosdal RM (eds) Structural Control on Ore Genesis.
1081 Rev Econ Geol 14:25–50
1082 Sinha M (1997) Gold mineralization in the western Ramagiri block, Anantapur
1083 district, Andhra Pradesh, with special reference to fluid inclusion characteristics.
1084 Unpublished MSc. Thesis Indian Institute of Technology Kharagpur.
1085 Smith TJ, Cloke PL, Kesler SE, (1984) Geochemistry and fluid inclusions from the
1086 McIntyre-Hollinger gold deposit, Timmins, Ontario, Canada Econ Geol
1087 79:1265–1285
1088 Smoliar MI, Walker RJ, Morgan JW (1996) Re-Os constraints on the age of Group
1089 IIA, IIIA, IVA, and IVB iron meteorites: Science 271:1099–1102
1090 Spooner ETC, Bray CJ, Wood PC, Burrows DR, Callan NJ (1987) Grant 236. Au-
1091 quartz vein and Cu-Au-Ag-Mo-Anydrite mineralization, Hollinger-McIntyre
1092 mines, Timmins, Ontario: $\delta^{13}C$ values (McIntyre), fluid inclusion gas chemistry,
1093 pressure (depth) estimation and H_2O-CO_2 phase separation as a precipitation and
1094 dilation mechanism. Ontario Geological Survey, Miscellaneous Paper 136:33–36
1095 Stipp M, Stunitz H, Heilbronner R, Schmid SM (2002) The eastern Tonale fault zone:
1096 A “natural laboratory” for crystal plastic deformation of quartz over a temperature
1097 range from 250 to 700ºC. J Struct Geol 24:1861–1884
1098 Thiéry R, Videl J, Dubessy J (1994) Phase equilibria modeling applied to fluid
1099 inclusions. Liquid–vapor equilibria and calculation of the molar volume in the
1100 CO_2-CH_4-N_2 system. Geochim Cosmochim Acta 58:1073–1082
1101 Thomas RJ, Verbeek JA, Walraven F (1995) Geology of the Archaean Nzimane
1102 Inlier, Zululand. Abstract, Centen. Geocongress Geol Soc South Afr pp 200–203
1103 Tomkin AG (2013) On the source of orogenic gold. Geology 41:1255–1256
1104 Touret JLR (2001) Fluid inclusions in metamorphic rocks. Lithos 55:1–25
1105 Vidal O, De Andrade V, Lewin E, Munoz M, Parra T, Pascarelli S (2006) P-T-
1106 deformation-Fe^{3+}/Fe^{2+} mapping at the thin section scale and comparison with

XANES mapping. Application to a garnet-bearing metapelite from the Sambagawa metamorphic belt (Japan). J Metamorphic Geol 24:669–683

Vidal O**,** Parra T, Trotet F (2001) A thermodynamic model for Fe-Mg aluminous chlorite using data from phase equilibrium experiments and natural pelitic assemblages in the 100-600°C, 1-25 kbar P-T range. Am J Sci 301:557–592

Vidal O, Parra T, Vieillard P (2005) Thermodynamic properties of the Tschermak solid solution in Fe-chlorites: Application to natural examples and possible role of oxidation. Am Mineral 90:359–370

Wilkinson JJ, Johnston JD (1996) Pressure fluctuations, phase separation, and gold precipitation during seismic fracture propagation. Geology 24:395–398

Wilson AC, Jackson MPA (1988) Mantled gneiss domes in southern Swaziland and the concept of 'stable' Pongola cratonic cover. S. Afr. J. Geol 91:404–414

Zang W Fyfe WS (1995) Chloritization of the hydrothermally altered bedrock at the Igarape Bahia gold deposit, Carajás, Brazil. Miner Depos 30:30–38

Zhang Y, Frantz JD (1987) Determination of homogenization temperature and densities of supercritical fluid in the system NaCl-KCl-$CaCl_2$-H_2O using synthetic fluid inclusions. Chem Geol 64:335–350

List of Figures

Fig. 1. (a) Locality map showing position of the main Pongola basin in South Africa. (b) Regional geological map of the Pongola basin showing major structural features (modified after Gold 2006). (c) Geological map of the Klipwal Gold Mine showing the Klipwal Shear Zone within rocks of the Mozaan Group (modified after Gold and Von Veh 1995). PR: Piet Retief; P: Pongola.

Fig. 2**.** (a) Subsurface geological cross section across the Klipwal Shear Zone showing disposition of various reefs and alteration halos (modified after Hilliard 2007). (b) Poles to the shear zone foliation; equal area lower hemisphere projection. See text for discussion.

Fig. 3. Field photographs from Klipwal mine area (a) showing old mine excavation with siltstone in footwall and sandstone in the hanging wall. (b) Slickensides (dashed lines) on the siltstone surfaces. (c) Shear related fold with NW trending axial planar fabric (broken line). (d) Sheared and mylonitized fabric in sandstone.

Fig. 4. Underground mine photographs showing different features of shear zone, laminated fault-fill quartz veins and alteration zones. (a) Laminated quartz vein in the inner zone preserving S-C fabric with sinistral sense of shear. (b) Oblique S-C fabric with sinistral sense of shear in the wall rock mylonites along with quartz shear lenses.

(c) Sub-horizontal extension vein arrays associated with fault-fill vein in the shear zone. (d) Fault gouge in the R-reef showing fault breccia with fragments of host rocks and quartz veins and mylonites. (e) Extensional veins are displaced by the later faults. (f) H-reef fault-fill quartz vein and mylonitic shear zone contact with absence of fault breccia.

Fig. 5. Geological map along a crosscut from the main drive (R-reef) at level 10 which cuts across H- and J- reefs. Stars denote the sample locations. The map shows underground geology, alteration halos around the reefs and the attitude of shear foliation in the quartz veins.

Fig. 6. Photomicrographs showing mineralogical and structural features of least altered and altered host rocks in the proximal zone. Photographs a to d, f: + Pol; e: plane-polarized light. See text for discussion. Mineral abbreviations are after Kretz (1983). Car: carbonates.

Fig. 7. Photomicrographs showing the mineralogical and structural features of the auriferous laminated quartz veins in the inner zone. (a) Alternating laminae consisting of quartz + dolomite and muscovite + chlorite. (b) S-C fabric within the lamina showing sinistral sense of shear. (c) Plastic deformation structures in quartz grains. (d) Quartz shear lens within the mylonites. (e) Fragments of quartz vein with brittle fractures and mylonite clasts in fault breccia. (f) Brittle fractures in the arsenopyrite and pyrite grains are filled with quartz and chlorite; quartz strain fringes with chlorite. (g) Silicate inclusion trails within sulfides showing relationship between sulfide growth and shear foliation. (h) Sketch of (g) for clear illustration. All photographs are taken under + Pol, except (e and g). See text for discussion. Mineral abbreviations are after Kretz (1983).

Fig. 8. Reflected light photomicrographs and BSE images showing different types of pyrites. (a) Three textural types of pyrite. (b) Coexisting pyrite-I and arsenopyrite-I along with pyrite-II inclusions within arsenopyrite-I. (c) Gold (Au) and chalcopyrite inclusions within pyrite-I with arsenopyrite-II at pyrite-I boundary. (d) Chalcopyrite, pyrrhotite and arsenopyrite-II inclusions within pyrite-II. (e) Euhedral pyrite-I grains with silicate inclusions and As-poor zone (dotted line). (f) Pyrite-II overgrows on pyrite-I (dotted line). (g) Concentric As-poor and As-rich zones in pyrite-II. (h) Irregular As zoning in pyrite-II. All photographs were taken in plane-polarized light. Mineral abbreviations are after Kretz (1983).

Fig. 9. Summary of different textural types of pyrite and arsenopyrite, in the inner and proximal alteration zone, with schematic sketches. Mineral abbreviations are after Kretz (1983)

Fig. 10. Reflected light photomicrographs in plane-polarized light showing occurrence of gold in the Klipwal deposit. (a) Gold (Au) inclusions within pyrite-I at the contact of chalcopyrite grain. (b) Gold as isolated inclusion within pyrite-I. (c) Inclusion of gold grain within arsenopyrite-II. (d) Free gold grain in quartz matrix, sharing the grain boundary with chlorite (Chl). Mineral abbreviations are after Kretz (1983).

Fig. 11. Representative photomicrographs and Raman spectra of different fluid inclusion types. (a) Isolated type-I inclusion. (b) Occurrence of type-II and type-III inclusions in the same 3-dimenstioanl cluster. (c) Representative Raman spectrum of type-II inclusions showing CH_4 peak at 2912 cm^{-1}. (d) Raman spectrum of type-III inclusions showing CO_2 doublets (at 1283 and 1388 cm^{-1}) and presence of CH_4 (at 2913 cm^{-1}). (e) Intra-granular trail of type-IV inclusions. (f) Coexisting type-III (C) and type-IV (A) inclusions in one group of synchronous inclusions (GSI).

Fig. 12. Histogram plots of fluid inclusion microthermometric data. (a) Temperatures of CH_4 vapor homogenization of type-II inclusions, (b) Temperatures CO_2 ice melting and (c) Homogenization of type-III inclusions, (d) Last ice melting and (e) Liquid vapor homogenization temperatures of type-IV inclusions, (f) $T_{h,CO2}$ versus $T_{m,CO2}$ plot for pure CO_2 type-III inclusions showing density variation.

Fig. 13. Isochore plot constructed using the minimum and maximum densities of each type of inclusions. Figures indicate the density values (in g/cm^3) for respective inclusions. P-T estimation by (i) intersecting isochores of type-III (solid lines) and type-IV (dashed lines) inclusions (ii) intersection of chlorite thermometer (CT) and (iii) arsenopyrite thermometer (AT) with the isochores. The box illustrates the P-T domain of gold mineralization at Klipwal. IS-1 and IS-2 denotes isochore intersection.

Fig. 14. $^{187}Re/^{188}Os$ vs. $^{187}Os/^{188}Os$ isochron plot for pyrite and arsenopyrite grains from the ore zone. See text for discussion.

Figure
Click here to download high resolution image

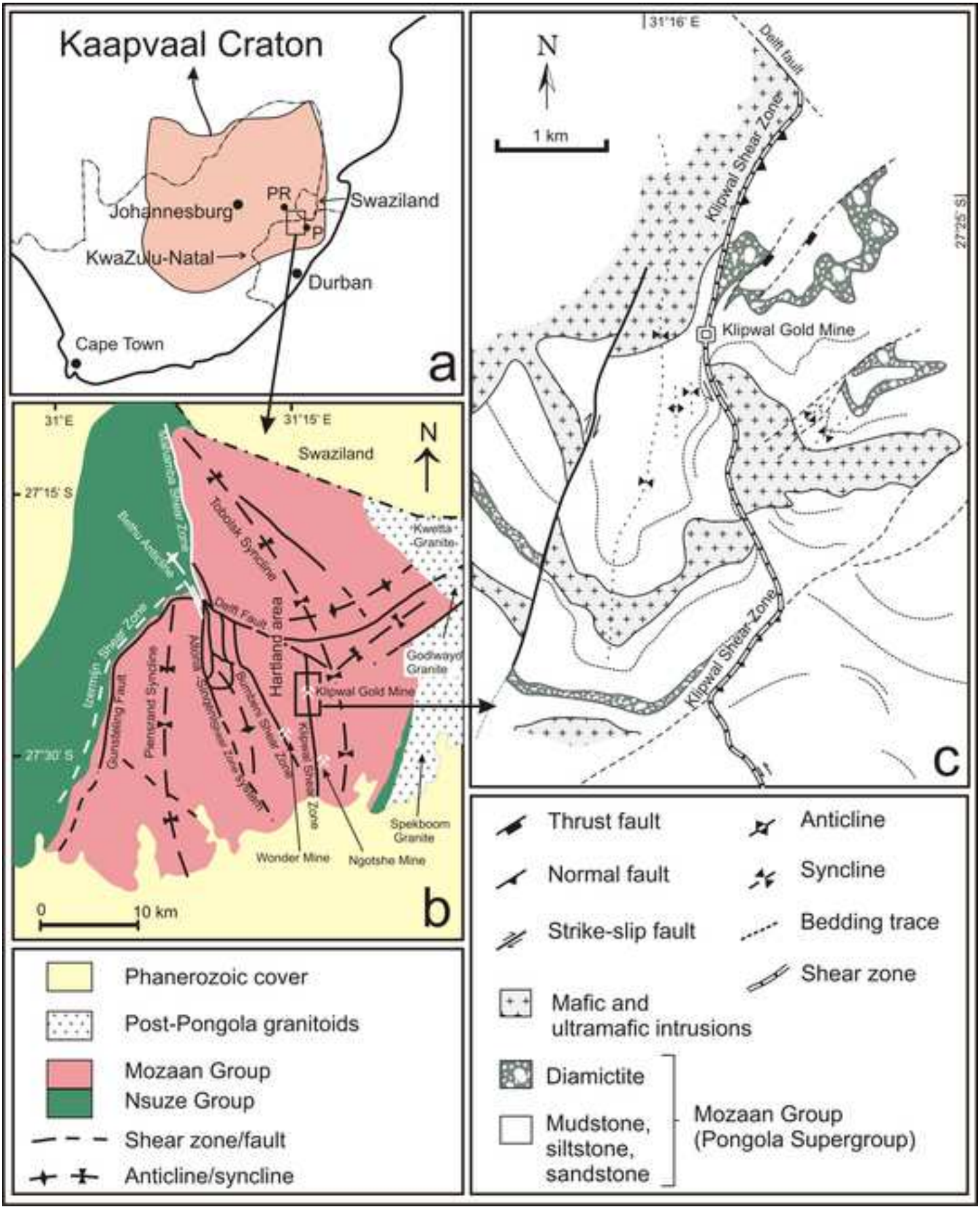

Figure
Click here to download high resolution image

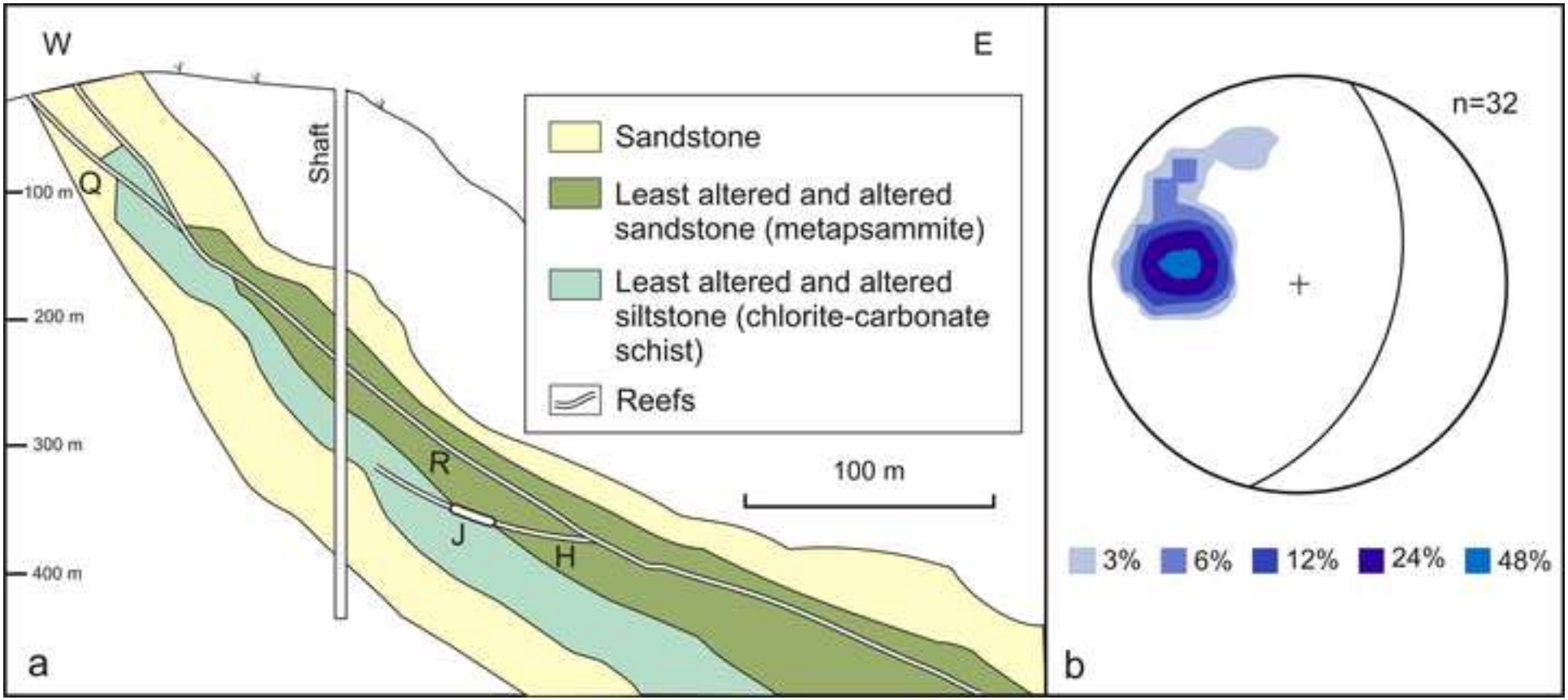

Figure
Click here to download high resolution image

Figure
Click here to download high resolution image

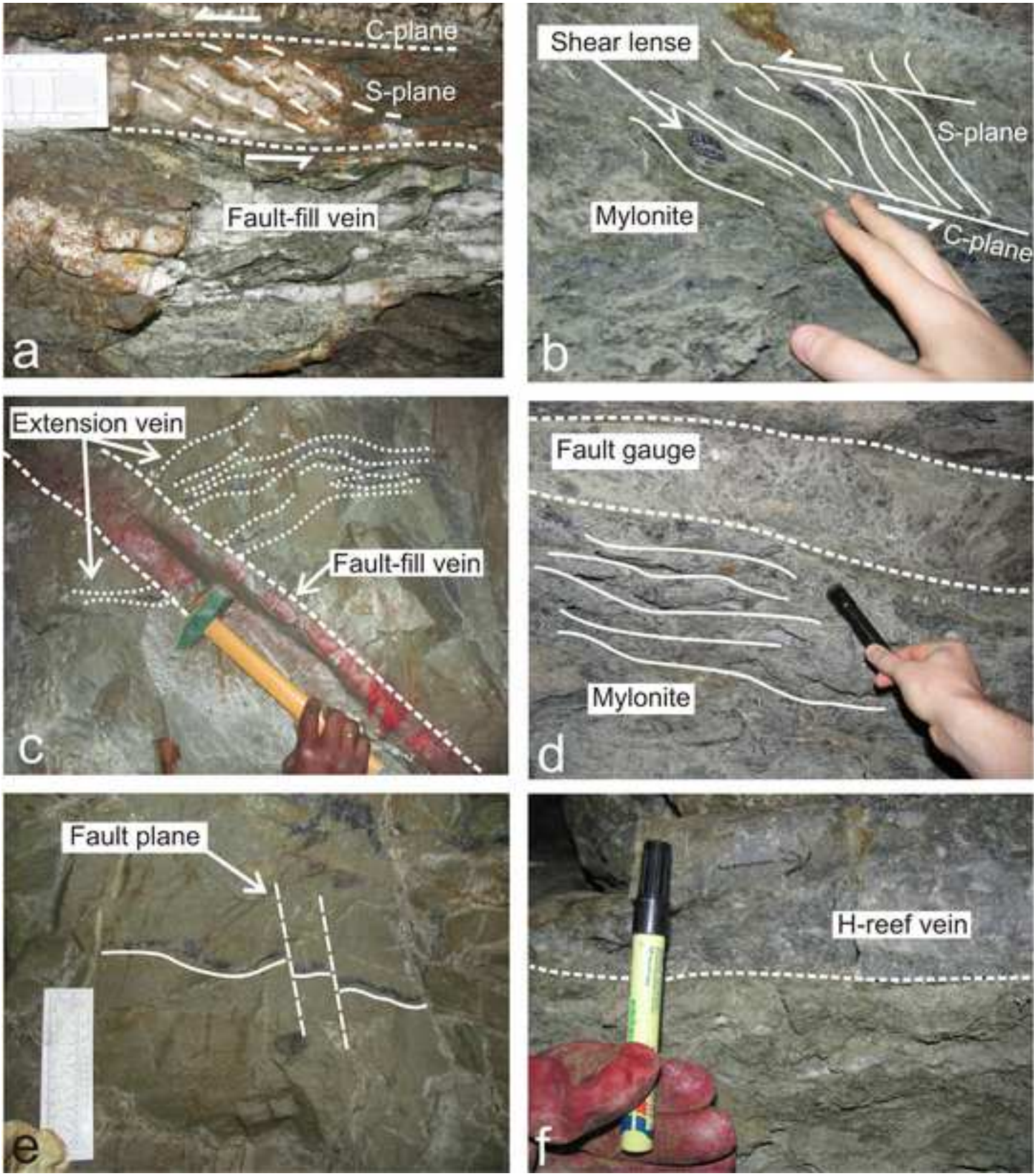

Figure
Click here to download high resolution image

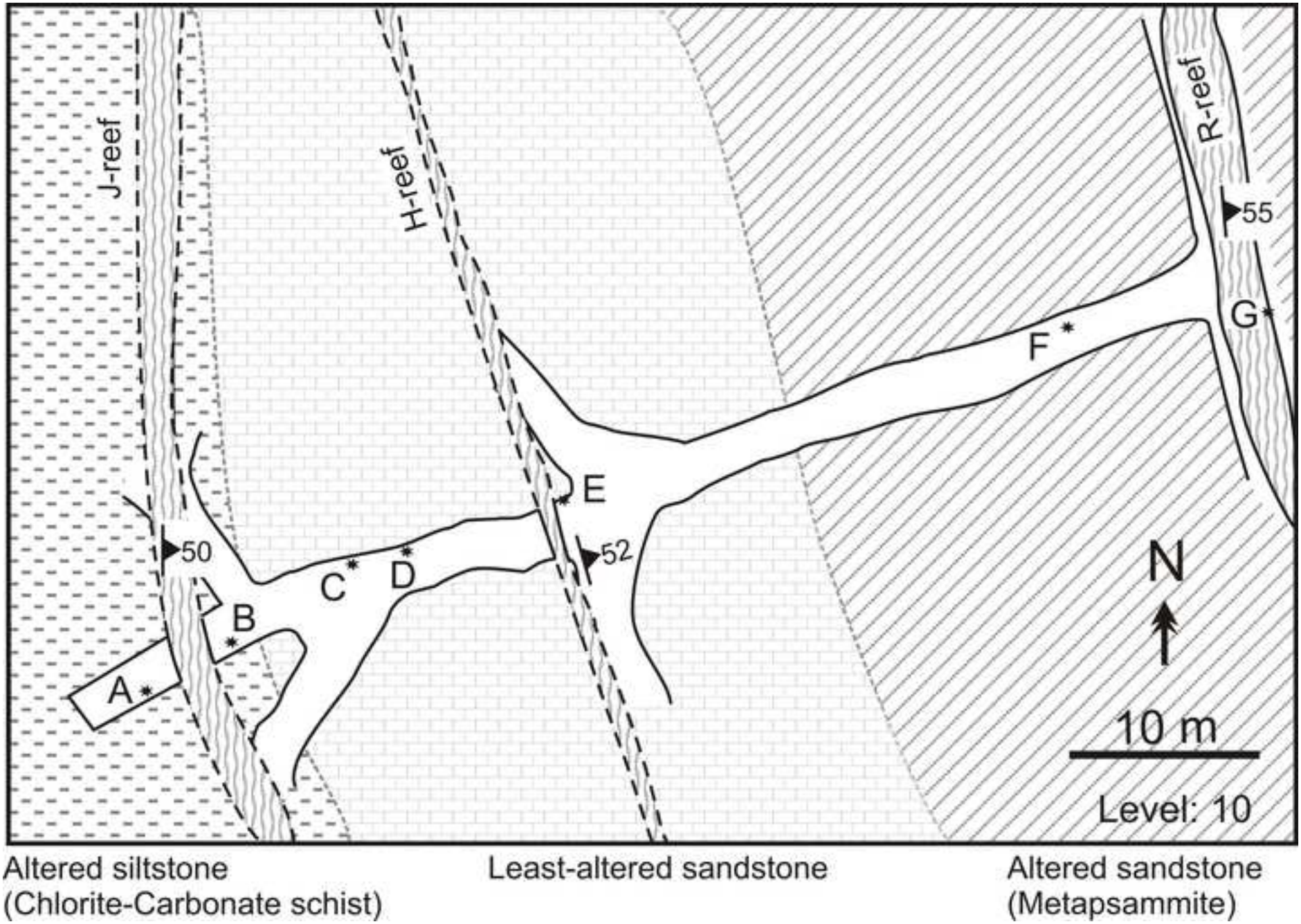

Figure
Click here to download high resolution image

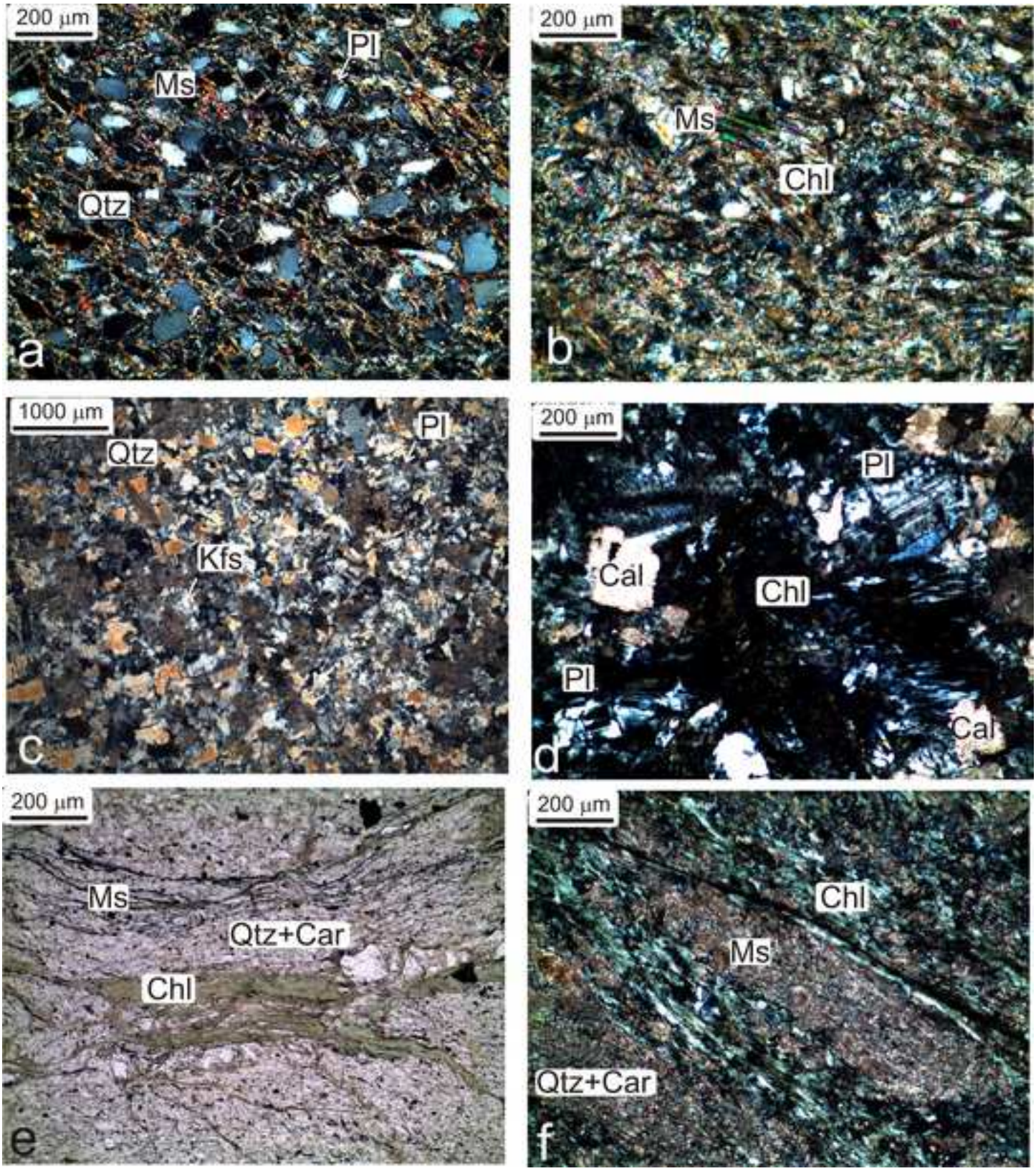

Figure
Click here to download high resolution image

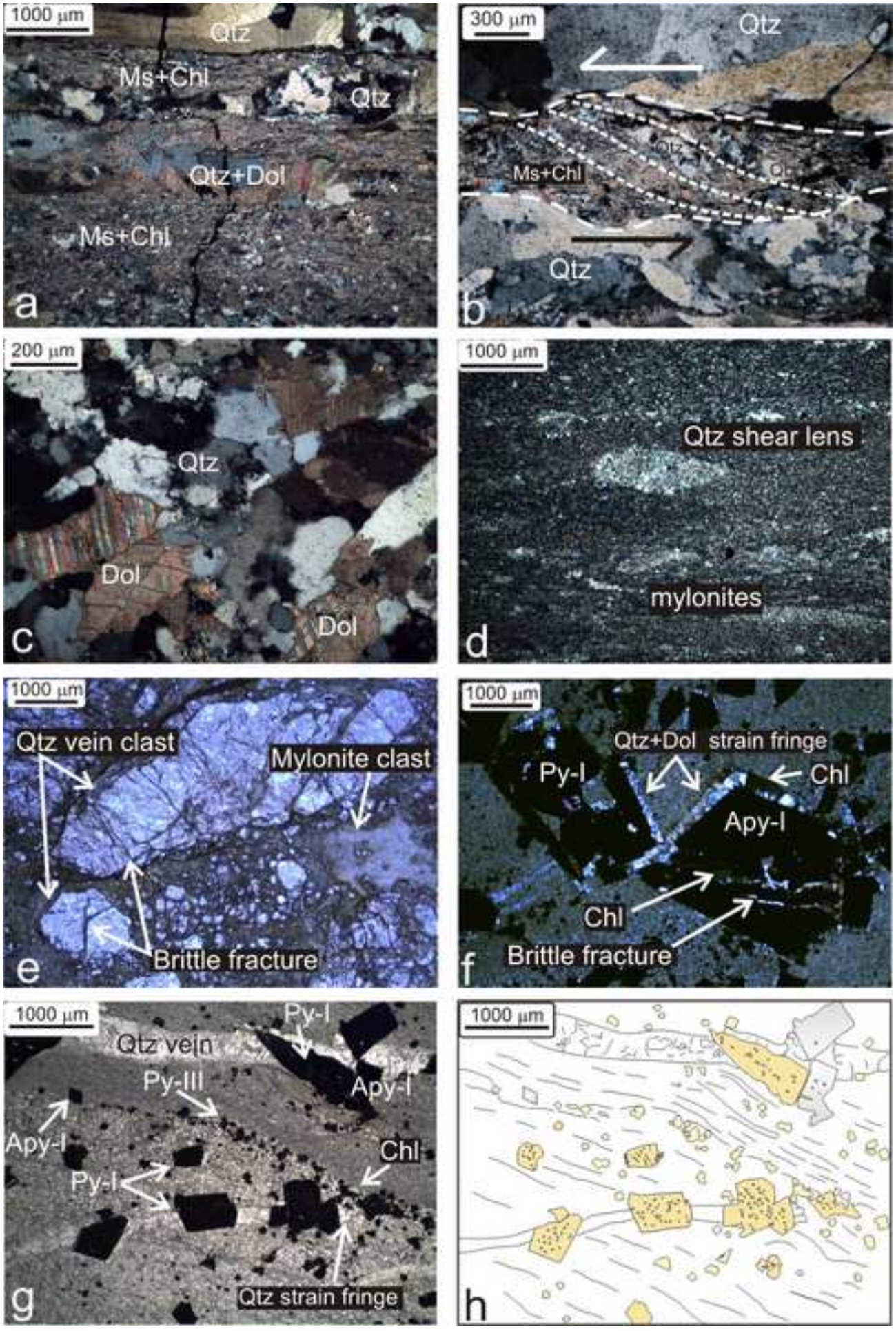

Figure
Click here to download high resolution image

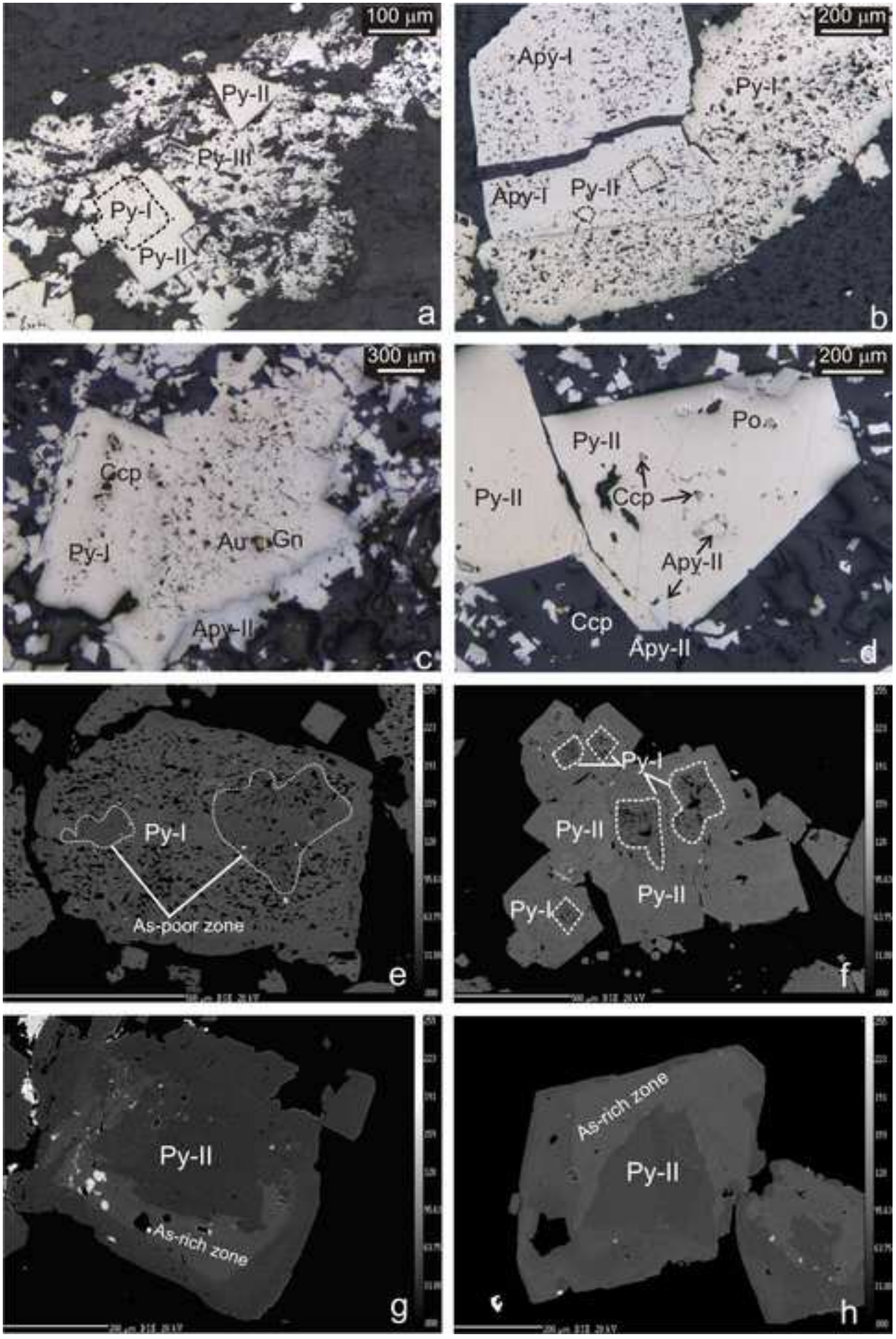

Figure
Click here to download high resolution image

Textural type	Description	Schematic sketch of texture
Arsenopyrite-I	Large euhedral grains with abundant randomly oriented silicate inclusions and may contain inclusions of pyrite-II	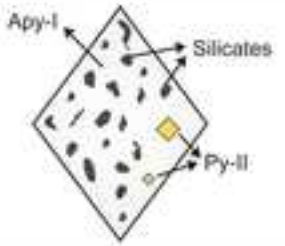
Pyrite-I	Euhedral in shape with numerous randomly to preferentially oriented silicates inclusions and may contain inclusions of sulfides and gold	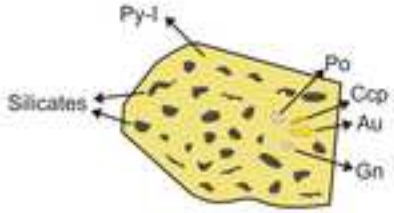
Pyrite-II	Euhedral pyrite, almost devoid of silicate inclusions and generally overgrow pyrite-I	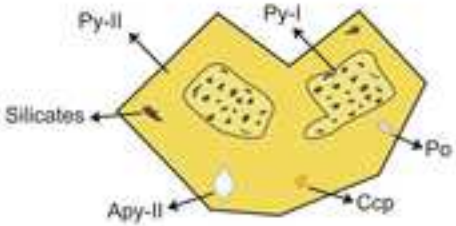
Arsenopyrite-II	Euhedral to subhedral in shape, smaller in size than arsenopyrite-I, free of any silicate inclusions and may overgrow pyrite-I	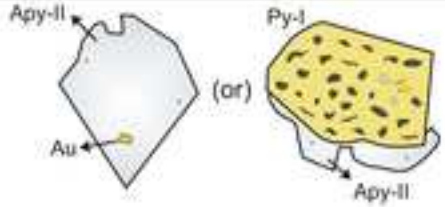
Pyrite-III	Irregular grain boundaries and overgrows the shear foliation.	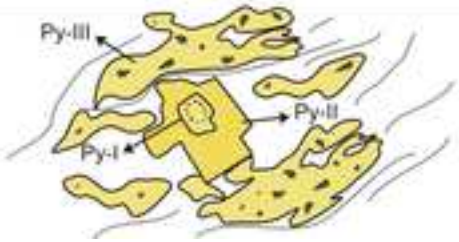

Figure
Click here to download high resolution image

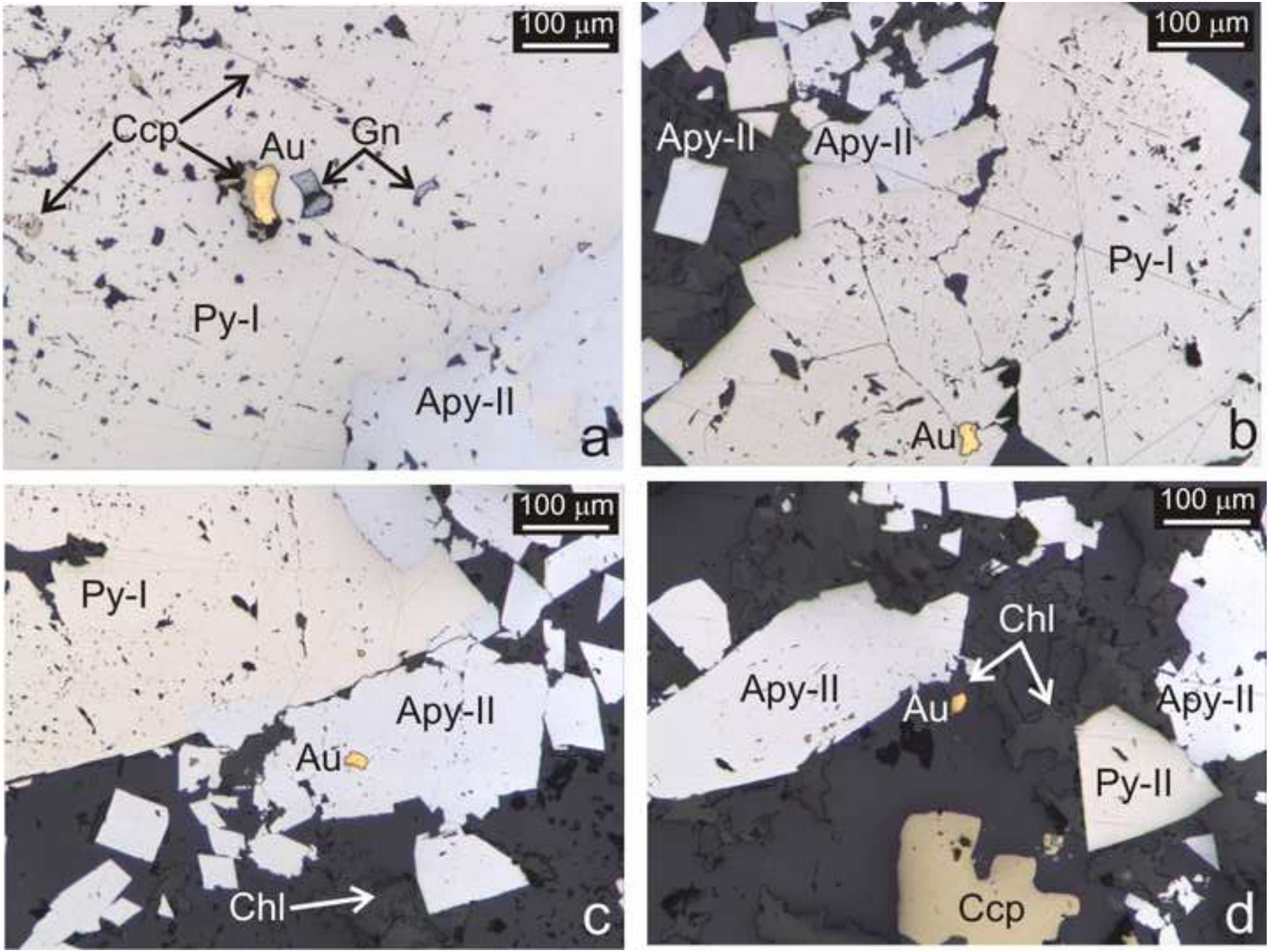

Figure
Click here to download high resolution image

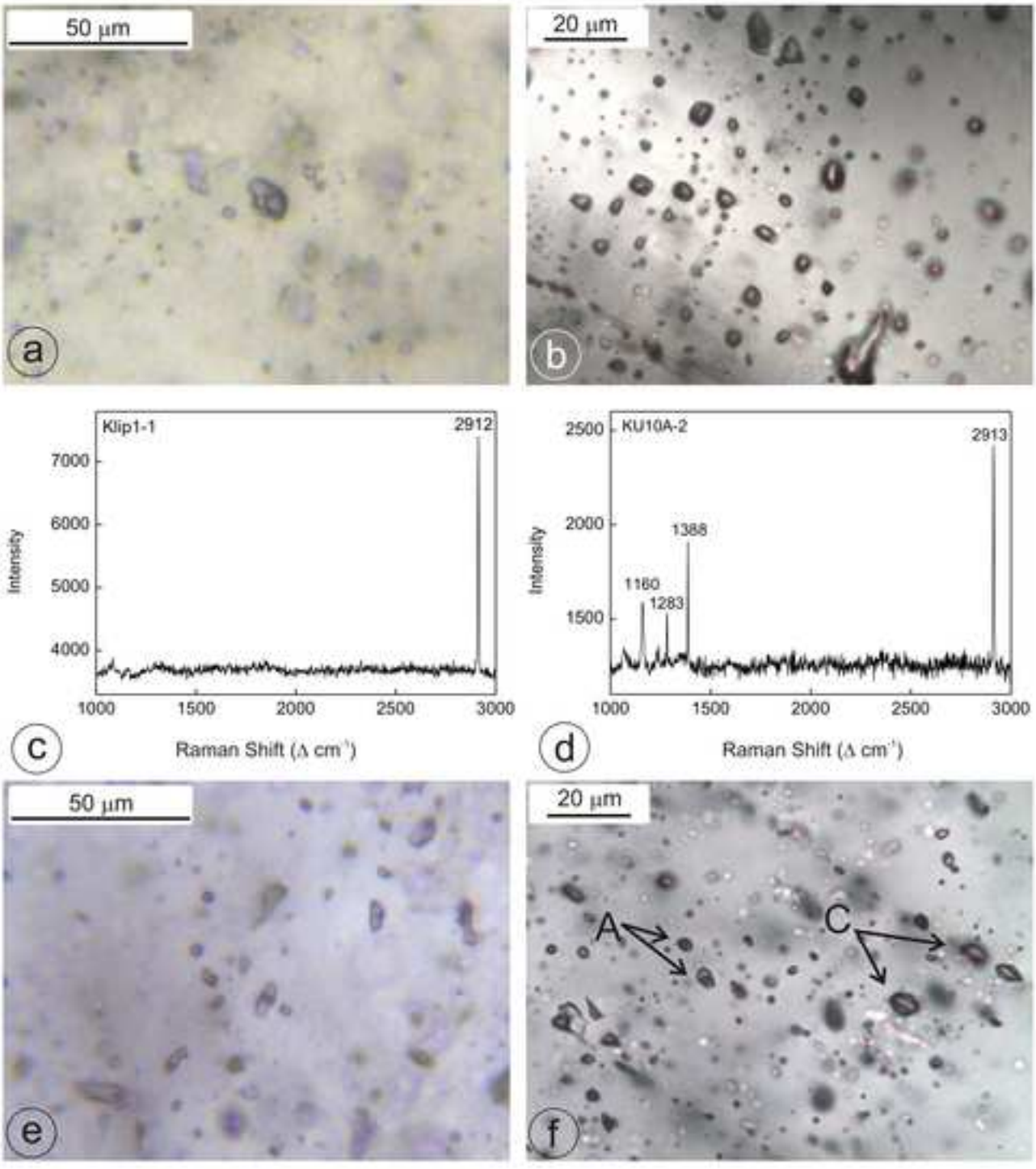

Figure
Click here to download high resolution image

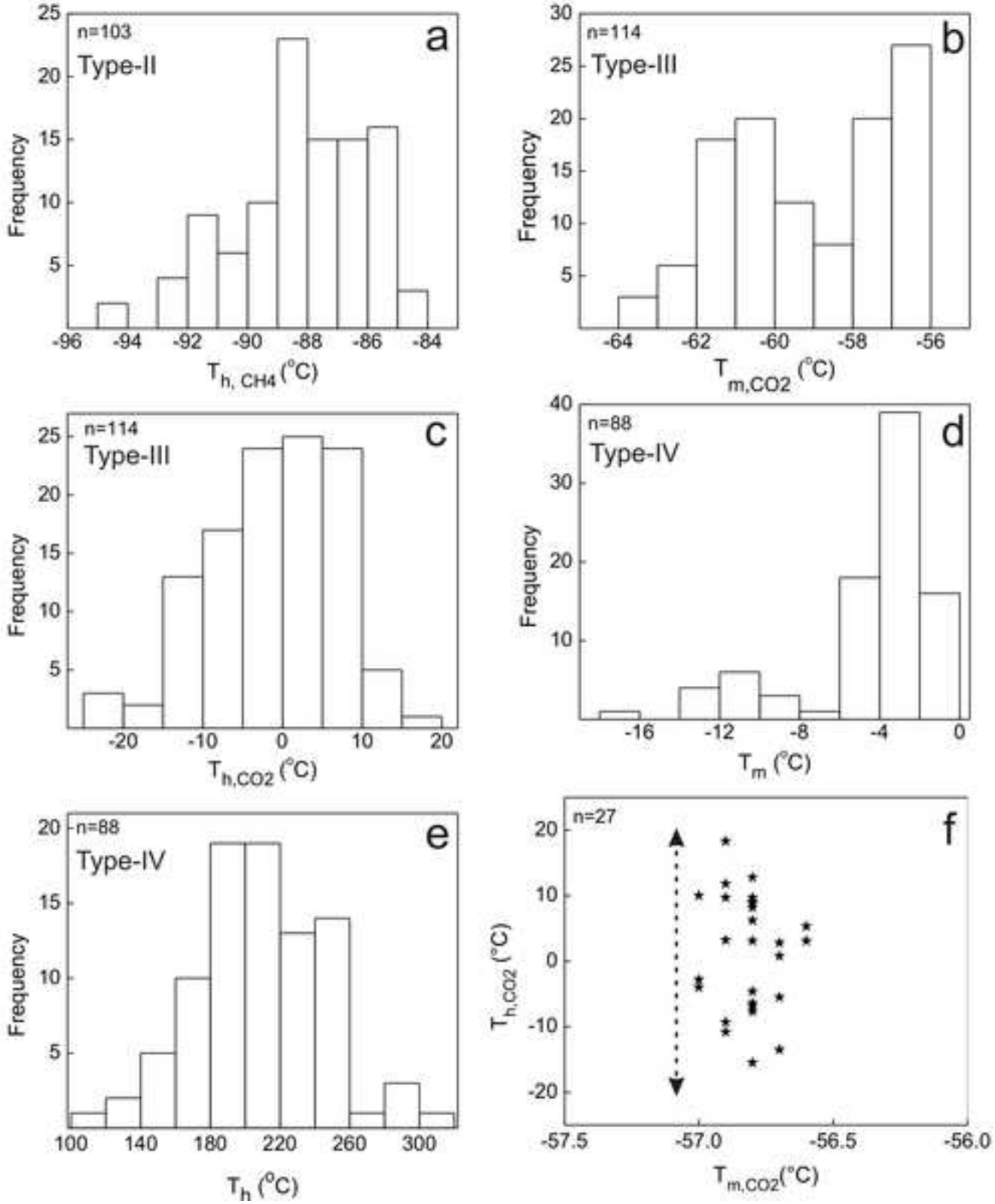

Figure
Click here to download high resolution image

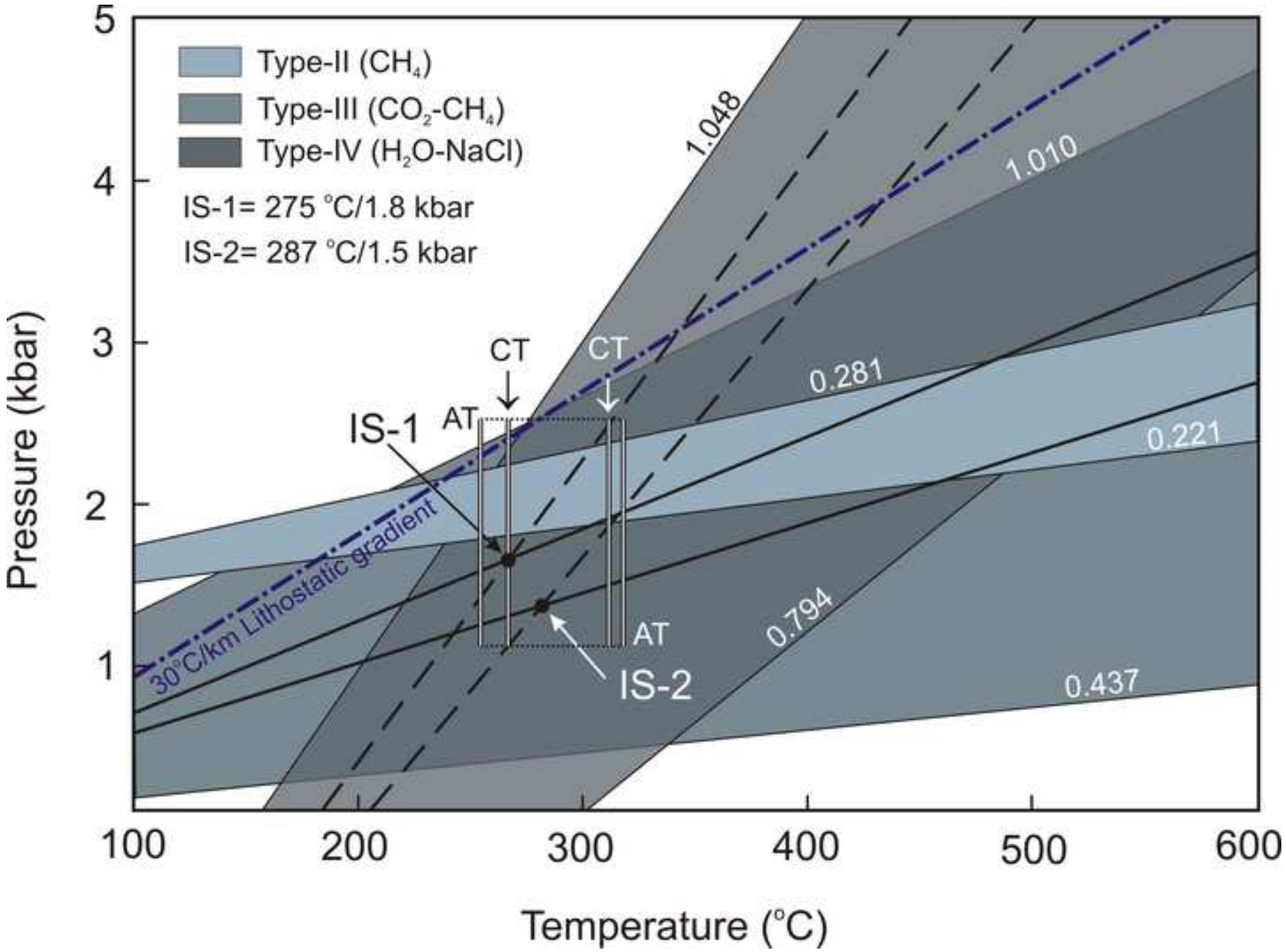

Figure
Click here to download high resolution image

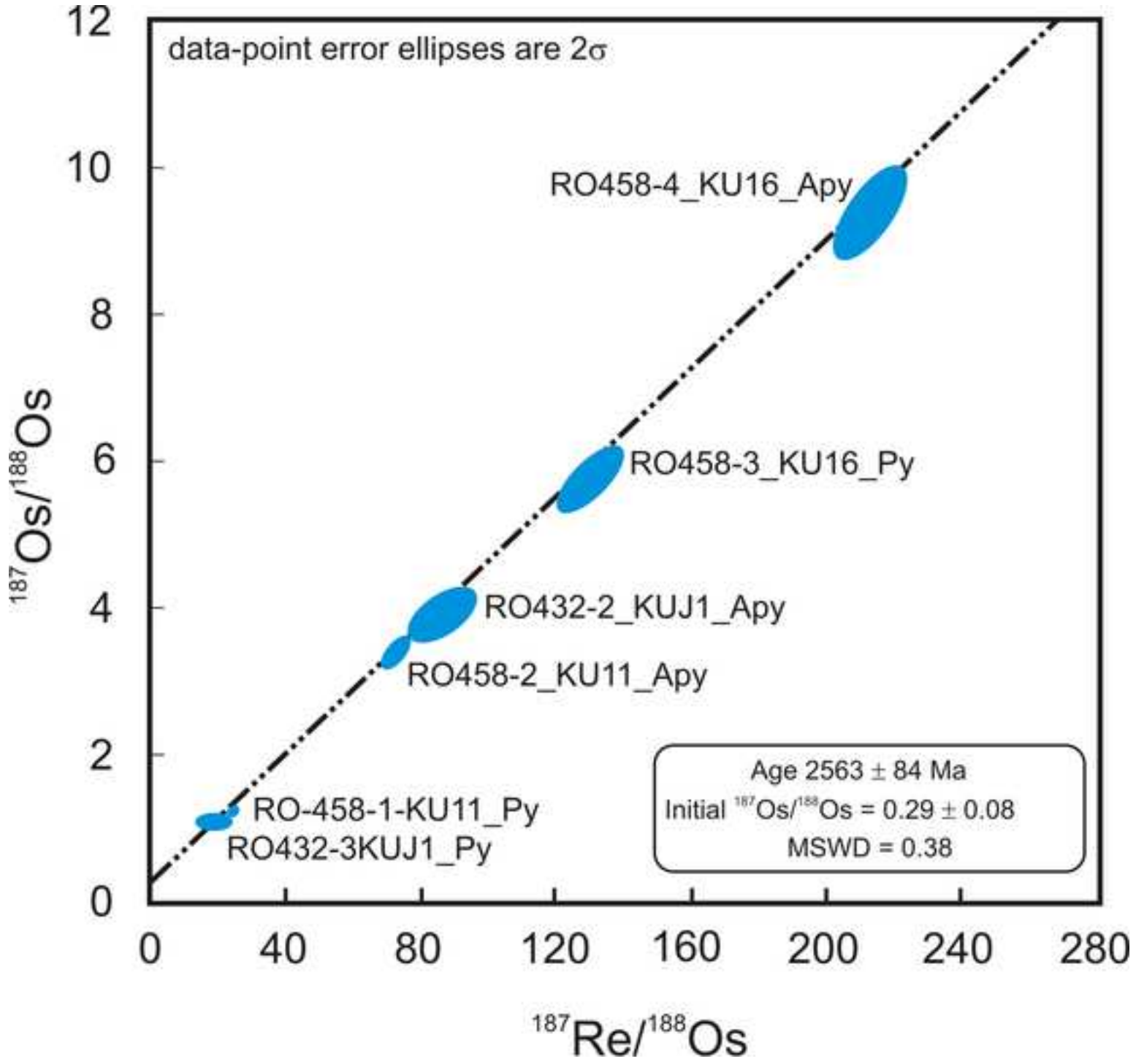

Table

Table. 1. Representative electron probe microanalytical data, structural formulae and estimated temperatures of chlorite from the alteration zones.

	R-reef												
Sample No	KU4B												
Analysis No	mat-1	mat-2	mat-4	mat-5	py-6	py-7	py-8	py-9	py-10	mat-11	mat-12	mat-13	mat-16
SiO_2	25.62	25.25	25.38	25.51	25.08	26.04	25.21	25.38	25.52	25.78	25.48	26.65	26.82
Al_2O_3	20.88	20.49	20.89	20.17	20.59	20.56	20.48	20.55	20.42	20.75	20.64	18.96	19.42
FeO	27.85	29.21	27.81	27.12	27.74	28.80	28.33	28.97	27.34	28.11	28.10	28.20	28.53
MnO	0.10	0.10	0.11	0.20	0.14	0.00	0.17	0.17	0.13	0.15	0.05	0.11	0.07
MgO	13.63	12.92	13.02	13.47	12.70	13.39	13.17	13.28	13.65	13.65	13.29	14.13	14.04
Total	88.08	87.97	87.21	86.47	86.25	88.79	87.36	88.35	87.06	88.44	87.56	88.05	88.88
Cations													
Si	2.70	2.67	2.72	2.69	2.67	2.69	2.67	2.67	2.69	2.70	2.67	2.73	2.74
Al	2.60	2.55	2.64	2.51	2.59	2.50	2.56	2.54	2.53	2.56	2.55	2.29	2.34
Fe(tot.)	2.46	2.58	2.49	2.39	2.47	2.48	2.51	2.54	2.41	2.46	2.47	2.42	2.43
Mn	0.01	0.01	0.01	0.02	0.01	0.00	0.02	0.02	0.01	0.01	0.00	0.01	0.01
Mg	2.14	2.03	2.08	2.12	2.02	2.06	2.08	2.08	2.14	2.13	2.08	2.16	2.14
Total	9.91	9.84	9.93	9.73	9.76	9.73	9.83	9.85	9.78	9.87	9.78	9.61	9.65
T1 (tetrahedral Al: CN85)	293	300	290	295	300	297	300	301	296	293	299	287	286
T2 (octahedral vacancy: CN85)	270	263	273	250	253	249	262	263	256	266	256	236	240
T3 (tetrahedral Al & Fe/(Fe+Mg): ZF95)	276	269	276	279	276	285	297	272	287	279	282	278	300
Avg. T °C	*280*	*278*	*280*	*275*	*276*	*277*	*286*	*279*	*280*	*280*	*279*	*267*	*276*
SD	12	20	9	23	23	25	21	20	21	14	22	27	31
Eq. (1)	286	300	287	304	308	312	300	309	300	287	309	300	278
Eq. (2)	317	303	328	292	300	299	306	312	299	308	301	279	269
Eq. (3)	300	300	305	299	306	306	302	310	300	297	306	291	276
Avg.T °C (T4) V01&05	*301*	*301*	*307*	*298*	*305*	*306*	*302*	*310*	*300*	*297*	*305*	*290*	*274*
SD	16	2	20	6	4	7	3	1	1	11	4	10	5
a(H_2O)	0.3	0.5	0.2	0.9	0.8	1.0	0.5	0.5	0.8	0.5	0.8	0.6	1.0

	R-reef														
Sample No	KU4G														
Analysis No	vein-1	vein-2	vein-3	vein-4	vein-5	vein-6	vein-7	vein-8	vein-9	vein-10	mat-11	mat-12	mat-13	mat-14	mat-15
SiO_2	24.25	24.23	24.33	24.16	24.23	24.18	24.27	24.49	24.70	24.50	24.37	24.85	24.60	24.38	22.93
Al_2O_3	18.46	18.81	18.82	18.35	18.87	18.72	18.82	18.61	18.51	18.37	18.96	19.33	18.38	18.93	18.03
FeO	36.32	36.69	36.91	36.25	36.49	36.50	36.50	36.32	36.45	36.62	36.68	36.78	37.15	36.44	35.33
MnO	0.13	0.04	0.01	0.08	0.09	0.08	0.11	0.12	0.09	0.19	0.06	0.16	0.05	0.00	0.33
MgO	7.78	7.62	7.56	7.79	7.74	7.67	7.68	7.97	8.06	7.90	7.75	8.26	7.59	7.90	7.36
Total	86.94	87.39	87.63	86.63	87.42	87.15	87.38	87.51	87.81	87.58	87.82	89.38	87.77	87.65	83.98
Cations															
Si	2.67	2.67	2.67	2.68	2.66	2.67	2.67	2.67	2.68	2.68	2.67	2.66	2.68	2.67	2.67
Al	2.39	2.44	2.44	2.40	2.45	2.44	2.44	2.39	2.37	2.37	2.45	2.44	2.36	2.45	2.47
Fe(tot.)	3.34	3.38	3.39	3.37	3.36	3.37	3.36	3.32	3.31	3.35	3.36	3.30	3.39	3.34	3.44
Mn	0.01	0.00	0.00	0.01	0.01	0.01	0.01	0.01	0.01	0.02	0.01	0.01	0.00	0.00	0.03
Mg	1.28	1.25	1.24	1.29	1.27	1.26	1.26	1.30	1.31	1.29	1.27	1.32	1.23	1.29	1.28
Total	9.69	9.74	9.74	9.75	9.74	9.75	9.74	9.69	9.68	9.69	9.75	9.74	9.68	9.75	9.89
T1 (tetrahedral Al: CN85)	301	300	299	297	301	300	300	299	297	299	300	301	297	300	300
T2 (octahedral vacancy: CN85)	245	251	251	252	251	252	251	246	244	245	252	251	244	252	269
T3 (tetrahedral Al& Fe/(Fe+Mg): ZF95)	302	303	304	305	306	307	308	309	310	311	312	313	314	315	316
Avg. T °C	*283*	*285*	*285*	*285*	*286*	*286*	*286*	*285*	*284*	*285*	*288*	*288*	*285*	*289*	*295*
SD	33	29	30	29	30	30	31	34	35	35	32	33	37	33	24
Eq. (1)	314	314	306	301	320	317	314	321	311	316	308	312	310	311	286
Eq. (2)	286	298	292	292	302	300	299	292	290	292	292	298	288	296	301
Eq. (3)	301	306	300	298	313	311	307	308	301	306	301	306	300	305	292
Avg.T °C (T4) V01&05	*301*	*306*	*299*	*297*	*312*	*309*	*307*	*307*	*300*	*305*	*300*	*305*	*299*	*304*	*293*
SD	14	8	7	5	9	9	8	14	10	12	8	7	11	8	8
a(H_2O)	0.8	1.0	1.0	1.0	1.0	1.0	1.0	0.9	1.0	0.9	0.9	0.9	1.0	1.0	0.3

	J reef				
Sample No	KU12B				
Analysis No	1	2	3	5	7
SiO_2	25.49	23.94	25.64	24.69	24.89
Al_2O_3	18.44	21.41	18.52	20.78	19.80
FeO	33.87	33.70	33.09	34.06	34.24
MnO	0.00	0.02	0.13	0.00	0.00
MgO	9.40	7.97	9.65	7.75	8.90
Total	87.20	87.04	87.03	87.28	87.83
Cations					
Si	2.74	2.66	2.84	2.68	2.68
Al	2.33	2.80	2.41	2.65	2.52
Fe(tot.)	3.04	3.13	3.06	3.09	3.09
Mn	0.00	0.00	0.01	0.00	0.00
Mg	1.50	1.32	1.59	1.25	1.43
Total	9.62	9.92	9.92	9.67	9.72
T1 (tetrahedral Al: CN85)	286	302	265	299	297
T2 (octahedral vacancy: CN85)	236	272	271	242	248
T3 (tetrahedral Al& Fe/(Fe+Mg): ZF95)	318	319	320	321	322
Avg. T °C	*280*	*298*	*286*	*288*	*289*
SD	41	24	30	41	38
Eq. (1)	279	277	247	299	291
Eq. (2)	264	296	323	274	279
Eq. (3)	273	284	277	288	285
Avg.T °C (T4) V01&05	*272*	*286*	*282*	*287*	*285*
SD	7	9	38	13	6
$a(H_2O)$	1.0	0.2	1.0	1.0	1.0

	J reef											
Sample No	KUJ1											
Analysis No	1	2	3	4	5	6	7	8	9	10	11	12
SiO_2	26.03	25.86	25.94	25.55	26.59	26.39	26.30	25.81	26.01	25.94	25.77	25.99
Al_2O_3	20.51	20.71	20.65	20.60	20.35	20.01	20.03	20.77	21.40	20.15	21.18	21.03
FeO	24.81	25.42	26.21	26.40	26.07	25.89	26.43	25.18	25.88	25.99	26.07	25.26
MnO	0.00	0.05	0.05	0.05	0.00	0.06	0.11	0.00	0.00	0.16	0.04	0.00
MgO	15.11	15.06	15.10	14.61	15.31	15.38	15.17	15.22	15.11	15.26	15.06	15.20
Total	86.46	87.10	87.95	87.21	88.32	87.73	88.04	86.98	88.40	87.50	88.12	87.48
Cations												
Si	2.70	2.68	2.72	2.68	2.71	2.70	2.70	2.71	2.70	2.72	2.69	2.69
Al	2.51	2.53	2.55	2.55	2.45	2.41	2.42	2.57	2.62	2.49	2.61	2.57
Fe(tot.)	2.15	2.21	2.30	2.32	2.22	2.22	2.27	2.21	2.25	2.28	2.28	2.19
Mn	0.00	0.00	0.00	0.00	0.00	0.01	0.01	0.00	0.00	0.01	0.00	0.00
Mg	2.34	2.33	2.36	2.28	2.33	2.35	2.32	2.38	2.34	2.39	2.35	2.35
Total	9.70	9.76	9.93	9.83	9.71	9.69	9.72	9.88	9.92	9.90	9.93	9.79
T1 (tetrahedral Al: CN85)	293	297	290	298	291	293	294	291	293	289	295	295
T2 (octahedral vacancy: CN85)	247	253	273	262	247	245	249	267	271	270	273	257
T3 (tetrahedral Al& Fe/(Fe+Mg): ZF95)	324	325	326	327	328	329	330	331	332	333	334	335
Avg. T °C	*288*	*292*	*296*	*296*	*289*	*289*	*291*	*297*	*299*	*297*	*301*	*296*
SD	39	36	27	33	41	43	41	33	31	33	31	39
Eq. (1)	300	278	287	283	269	281	277	282	297	262	299	274
Eq. (2)	287	276	325	296	268	268	275	307	323	299	327	279
Eq. (3)	295	277	304	289	268	276	276	292	307	277	311	276
Avg.T °C (T4) V01&05	*294*	*277*	*305*	*289*	*268*	*275*	*276*	*294*	*309*	*279*	*312*	*276*
SD	6	1	19	6	1	6	1	13	13	19	14	3
a(H_2O)	1.0	0.6	0.2	0.4	0.8	0.7	0.7	0.5	0.3	0.3	0.3	0.2

Note: CN85: Cathelineau and Nieva (1985); ZF95: Zang and Fyfe (1995); V01&05: Vidal et al. (2001) and (2005)

Table

Table. 2. Selected electron probe microanalytical data of arsenopyrite from alteration zones along with results of arsenopyrite thermometry after Kretschmar and Scot (1976) and Sharp et al. (1985).

Sample No	KU10A																		
Analysis No	2	3	4	8	11	12	13	14	16	17	18	22	23	25	26	27	28	30	31
Fe	36.12	36.26	36.47	36.63	36.65	36.77	36.37	36.26	36.35	36.47	36.82	36.55	36.55	36.72	36.14	36.67	36.82	36.33	36.57
As	41.46	40.85	41.06	41.08	41.55	41.20	41.77	40.85	42.10	42.09	41.05	41.28	41.75	41.61	42.45	41.29	41.10	41.16	40.99
S	22.72	22.68	22.90	22.80	22.52	22.59	22.40	22.90	22.34	22.22	22.74	22.55	22.39	22.45	21.97	22.86	22.95	22.75	22.84
Co	0.04	0.00	0.00	0.04	0.02	0.02	0.00	0.00	0.00	0.00	0.00	0.00	0.01	0.00	0.01	0.00	0.00	0.00	0.01
Ni	0.11	0.00	0.00	0.00	0.11	0.00	0.01	0.00	0.01	0.00	0.00	0.00	0.00	0.00	0.00	0.00	0.00	0.00	0.00
Cu	0.00	0.00	0.00	0.00	0.00	0.00	0.02	0.00	0.00	0.00	0.00	0.01	0.00	0.00	0.00	0.00	0.00	0.00	0.00
Zn	0.00	0.00	0.00	0.00	0.00	0.00	0.03	0.00	0.00	0.00	0.00	0.00	0.00	0.00	0.00	0.00	0.01	0.00	0.00
Ga	0.00	0.00	0.01	0.00	0.03	0.01	0.00	0.01	0.03	0.01	0.01	0.00	0.00	0.00	0.00	0.00	0.00	0.00	0.00
Se	0.16	0.18	0.10	0.18	0.18	0.15	0.12	0.17	0.18	0.13	0.13	0.14	0.14	0.15	0.13	0.22	0.15	0.17	0.15
Ag	0.00	0.00	0.00	0.00	0.00	0.00	0.00	0.00	0.01	0.00	0.01	0.00	0.00	0.00	0.00	0.01	0.00	0.00	0.00
Au	0.00	0.00	0.00	0.07	0.00	0.00	0.00	0.00	0.01	0.00	0.01	0.05	0.00	0.00	0.00	0.00	0.00	0.00	0.04
Total	100.61	99.98	100.54	100.78	101.05	100.73	100.73	100.19	101.03	100.92	100.76	100.58	100.83	100.92	100.69	101.05	101.03	100.42	100.61
As %	28.9	28.6	28.6	28.6	28.9	28.7	29.2	28.5	29.4	29.4	28.6	28.8	29.1	29.0	29.8	28.6	28.5	28.7	28.5
T (°C)	277	265	265	265	277	267	291	260	300	300	265	272	286	282	318	265	260	267	260

Sample No	KU16										
Analysis No	3	4	5	6	8	10	11	13	16	17	19
Fe	36.02	35.91	36.23	35.86	36.35	36.31	36.34	35.54	36.24	36.14	36.43
As	41.40	41.11	41.10	41.20	41.19	40.85	40.89	40.74	41.54	40.91	40.85
S	22.29	22.57	22.59	22.51	22.54	22.75	22.54	22.71	22.13	22.69	22.64
Co	0.00	0.02	0.00	0.01	0.00	0.01	0.01	0.01	0.00	0.00	0.00
Ni	0.00	0.01	0.00	0.00	0.00	0.00	0.00	0.00	0.00	0.00	0.00
Cu	0.00	0.00	0.00	0.00	0.00	0.00	0.00	0.00	0.00	0.00	0.00
Zn	0.00	0.00	0.00	0.00	0.00	0.00	0.00	0.00	0.00	0.00	0.00
Ga	0.00	0.00	0.00	0.00	0.00	0.00	0.02	0.00	0.00	0.02	0.04
Se	0.13	0.15	0.13	0.17	0.15	0.17	0.13	0.09	0.17	0.16	0.16
Ag	0.00	0.00	0.00	0.00	0.00	0.00	0.00	0.00	0.00	0.00	0.00
Au	0.00	0.00	0.04	0.00	0.00	0.03	0.00	0.00	0.00	0.04	0.03
Total	99.84	99.77	100.09	99.75	100.23	100.12	99.93	99.08	100.08	99.97	100.14
As %	29.0	28.8	28.7	28.8	28.7	28.4	28.5	28.6	29.1	28.5	28.4
T (°C)	282	272	262	272	262	255	260	265	286	260	255

Table

Table. 3. Summary of fluid inclusion microthermometric data.

Sample No (Reef)	Type	n	$T_{m,CO2}$ (°C)	$T_{h,CO2}$ (°C)	$T_{h,CH4}$ (°C)	$T_{m,Cl}$ (°C)	$T_{m,ice}$ (°C)	T_h (°C)	$T_{h,tot}$ (°C)	$X_{(CO2)}$	$X_{(CH4)}$	V_g(%)	Density (g/cm^3)
Klip-1 (R-reef)	I	12	-62.5 to -57.8	-12.6 to 7.8		9.2 to 13.5			299 to 367	0.25 to 0.75	0.03 to0.25	40 to 90	0.356 to 0.805
	II	31			-92.8 to -84.3					0.00	1.00		0.221 to 0.275
	III	33	-62.8 to -56.6	-13.1 to 9.1						0.73 to 1.0	0.27 to 0.0		0.663 to 0.971
	IV	22					-16.1 to -0.2	115 to 292					0.799 to 1.048
KU16 (R-reef)	II	20			-94.3 to -85.2								0.230 to 0.281
	III	25	-63.5 to-56.8	-15.5 to 18.3						0.69 to 1	0 to 0.31		0.690 to 1.010
	IV	19					-4.6 to -1.9	172 to 299					0.794 to 0.947
KU10A (J-reef)	I	9	-63.2 to -58.2	-15.2 to 0.5		7.8 to 14.8			272 to 345	0.71 to 0.95	0.05 to 0.29	70 to 90	0.352 to 0.713
	II	12			-91.9 to -84.8								0.226 to 0.271
	III	17	-63.9 to -60.0	-20.1 to 0.2									0.642 to 0.831
	IV	15					-10.3 to -0.3	205 to 302					0.803 to 0.935
KU12D (J-reef)	II	25			-94.2 to -85.4								0.232 to 0.280
	III	19	-60.2 to -56.7	-13.5 to 13.4						0.86 to 1.0	0.0 to 0.14		0.437 to 1.001
	IV	15					-12.2 to -2.0	157 to 222					0.901 to 0.982
KU9C (H-reef)	II	15			-92.5 to -84.9								0.227 to 0.273
	III	20	-63.0 to -57.2	-14.8 to 13.0						0.72 to 0.99	0.01 to 0.29		0.645 to 0.972
	IV	17					-12.5 to -0.5	130 to 250					0.831 to 1.022

Table

Table 4. Re-Os pyrite and arsenopyrite data.

Sample No	Location	Mineral	Re (ppb)	±	Os (ppt)	±	^{192}Os (ppt)	±	^{187}Re/^{188}Os	±	^{187}Os/^{188}Os	±	rho
RO432-2_KUJI_Apy	J-Reef	Arsenopyrite	0.9	0.1	73.4	2.4	20.3	1.4	84.1	8.1	3.9337	0.3161	0.626
RO432-3_KUJI_Py	J-Reef	Pyrite	0.2	0.1	56.6	1.7	20.7	1.5	18.7	5.7	1.1147	0.0905	0.193
RO458-1_KU11_Py	H-Reef	Pyrite	0.4	0.0	106.6	2.2	38.3	1.6	22.4	1.2	1.2645	0.0725	0.552
RO458-2_KU11_Apy	H-Reef	Arsenopyrite	1.6	0.0	154.1	3.9	44.4	1.8	70.6	3.0	3.4446	0.1967	0.692
RO458-3_KU16_Py	R-Reef	Pyrite	0.5	0.0	32.5	1.0	7.7	0.4	128.1	8.1	5.7947	0.3978	0.715
RO458-4_KU16_Apy	R-Reef	Arsenopyrite	4.7	0.0	240.4	8.0	44.8	1.8	210.4	8.6	9.4437	0.5389	0.708

Note: Uncertainties are reported at the 2σ level. ^{187}Os/^{188}Os uncertainties are at 2SE. All data are blank corrected, blanks for Os and Re were 0.1 ± 0.1 and 6.2 ± 5.4 ppt respectively, with an average ^{187}Os/^{188}Os value of 0.25 ± 0.02 (1 SD, n = 2).

Table

Table. 5. Summery of ore fluid compositions and P-T conditions of gold mineralization in major orogenic gold deposits around the world.

Age	Gold fields/ deposits	Cratons/regions	Fluid composition	Salinity (wt.% NaCl equiv.)	Mineralizing P-T conditions	References
Early Paleocene – Early Eocene	Alaska–Juneau, Treadwell Kensington	Juneau gold belt, SE Alaska	H_2O-CO_2-CH_4-NaCl	NA	250 to 350°C and 0.75 to 3 kbar	Goldfarb et al. (1993)
Siluro-Devonian	Hodgkinson gold field	NE Austraila,		3 to 11	270 to 355°C and ~1 kbar	Peters et al. (1990); Bierlein and Crowe (2000)
Cambro-Orodovician	Lachlan gold field	SE Australia		NA	250 to 350°C	Gao and Kwak (1995a, b); Ramsay et al. (1998)
Late – Middle Archaean	Willuna gold camp	Yilgarn Craton, western Australia	H_2O-CO_2-CH_4-NaCl with varying CO_2-CH_4 ratio	2.9±2.1	300±30°C and 0.55 to 1.4 kbar	Hagemann et al. (1994, 1996)
	Kalgoorlie camp, Golden Mile			NA	264 to 360°C and 1.5 to 2.3 kbar.	Ho (1987); Ho et al. (1990); Hagemann and Cassidy (2000)
	Mount Charlotte deposit			≤5		Hagemann and Cassidy (2000); Mernagh (1996)
	Hollinger-McIntyre deposit	Abitibi sub-province at Timmins district, Canada	H_2O-CO_2-CH_4-NaCl	NA	277±48°C	Smith et al. (1984); Spooner et al. (1987)
	Sigma-Lamaque, Val d'Or		H_2O-CO_2-CH_4-NaCl with 15–30 mole % CO_2	<10	1.8 to 2.6 kbar	Hagemann and Brown (1996); Robert and Kelly (1987)
	Barberton greenstone belt	Kappval Craton, South Africa	H_2O-CO_2-CH_4-NaCl	NA	~300°C and 1 kbar.	de Ronde et al. (1992)
	Kolar gold field	Eastern Dharwar Craton, India	H_2O-CO_2-NaCl	~7	205 to 280°C and 0.7 to 1.8 kbar	Mishra and Panigraghi (1999)
	Hutti gold mine, Hutti-Muski greenstone belt		H_2O-CO_2-CH_4-NaCl	3.9–13.5	280–320°C and 1.0 to 1.7 kbar	Pal and Mishra (2002); Mishra and Pal (2008)
	Hira-Buddini mine, Hutti-Muski greenstone belt			0.5 to 22.7	550°C[1] 320°C[2]	[1]Krienitz et al. (2008) [2]Mishra and Pal (2008)
	Ramagiri gold field		Dominantly carbonic fluids	low-salinity	1.45 kbar/240°C to 1.7 kbar/267°C;	Sinha (1997)
	Jonnagiri Deposit, Jonnagiri greenstone belt		H_2O-CO_2-CH_4-NaCl	~5	263 – 323°C and 1.4 to 2.5 kbar	Saravanan et al. (2009); Chinnasamy and Mishra (2013)

Note: NA= Not available